Blood vessel-based liver segmentation using the portal phase of an abdominal CT dataset

Ahmed S. Maklad
Systems Innovation Engineering, Graduate School of Advanced Technology and Science, The University of Tokushima, Tokushima 770-8506, Japan

Mikio Matsuhiro, Hidenobu Suzuki, Yoshiki Kawata, and Noboru Niki[a)]
Institute of Technology and Science, the University of Tokushima, Tokushima 770-8506, Japan

Mitsuo Satake
National Cancer Center Hospital East, Kashiwa, Chiba 277-8577, Japan

Noriyuki Moriyama
Tokyo Midtown Clinic, Minato-ku, Tokyo 107-6206, Japan

Toru Utsunomiya and Mitsuo Shimada
Institute of Health Biosciences, the University of Tokushima, Tokushima 770-8503, Japan

(Received 7 March 2013; revised 12 September 2013; accepted for publication 12 September 2013; published 11 October 2013)

Purpose: Blood vessel (BV) information can be used to guide body organ segmentation on computed tomography (CT) imaging. The proposed method uses abdominal BVs (ABVs) to segment the liver through the portal phase of an abdominal CT dataset. This method aims to address the wide variability in liver shape and size, separate liver from other organs of similar intensity, and segment hepatic low-intensity tumors (LITs).

Methods: Thin ABVs are enhanced using three-dimensional (3D) opening. ABVs are extracted and classified into hepatic BVs (HBVs) and nonhepatic BVs (non-HBVs) with a small number of interactions, and HBVs and non-HBVs are used for constraining automatic liver segmentation. HBVs are used to individually segment the core region of the liver. To separate the liver from other organs, this core region and non-HBVs are used to construct an initial 3D boundary surface. To segment LITs, the core region is classified into non-LIT- and LIT-parts by fitting the histogram of the core region using a variational Bayesian Gaussian mixture model. Each part of the core region is extended based on its corresponding component of the mixture, and extension is completed when it reaches a variation in intensity or the constructed boundary surface, which is reconfirmed to fit robustly between the liver and neighboring organs of similar intensity. A solid-angle technique is used to refine main BVs at the entrances to the inferior vena cava and the portal vein.

Results: The proposed method was applied to 80 datasets: 30 Medical Image Computing and Computer Assisted Intervention (MICCAI) and 50 non-MICCAI; 30 datasets of non-MICCAI data include tumors. Our results for MICCAI-test data were evaluated by sliver07 (http://www.sliver07.org/) organizers with an overall score of 85.7, which ranks best on the site as of July 2013. These results (average $\pm$ standard deviation) include the five error measures of the 2007 MICCAI workshop for liver segmentation as follows. Results for volume overlap error, relative volume difference, average symmetric surface distance, root mean square symmetric surface distance, and maximum symmetric surface distance were 4.33 ± 0.73, 0.28 ± 0.87, 0.63 ± 0.16, 1.19 ± 0.28, and 14.01 ± 2.88, respectively; and when applying our method to non-MICCAI data, results were 3.21 ± 0.75, 0.06 ± 1.29, 0.45 ± 0.17, 0.98 ± 0.26, and 12.69 ± 3.89, respectively. These results demonstrate high performance of the method when applied to different CT datasets.

Conclusions: BVs can be used to address the wide variability in liver shape and size, as BVs provide unique details for the structure of each studied liver. Constructing a boundary surface using HBVs and non-HBVs can separate liver from its neighboring organs of similar intensity. By fitting the histogram of the core region using a variational Bayesian Gaussian mixture model, LITs are segmented and measuring the volumetry of non-LIT- and LIT-parts becomes possible. Further examination of the proposed method on a large number of datasets is required for clinical applications, and development of the method for full automation may be possible and useful in the clinic. © *2013 American Association of Physicists in Medicine.* [http://dx.doi.org/10.1118/1.4823765]

Key words: liver segmentation, blood vessel (BV), boundary surface, computed tomography (CT) dataset, portal phase

1. INTRODUCTION

Liver segmentation is the basis for computer-based planning of surgical interventions.[1,2] Accurate preoperative estimates of graft weight are imperative to avoid small-for-size syndrome in the recipient and ensure donor safety after adult living donor liver transplantations.[1] Preoperative detailed topography as well as precise liver resection volume measurements should be obtained for curative hepatectomies.[2]

Manual segmentation is available clinically, but it is a tedious and time-consuming process that by its nature is not reproducible.[1] Nonmanual approaches for segmenting the liver are either automatic, semiautomatic, or interactive. Automatic approaches are desirable and have an additional advantage to semiautomatic and interactive methods in that automatic approaches have no user interactions; however, semiautomatic and interactive approaches remain essential for clinical settings especially with a very deformable organ like the liver.

For a comparison of different algorithms to segment the liver from clinical three-dimensional (3D) CT scans, Heimman *et al.*[3] started an investigation of 3D segmentation in the clinic: A grand challenge workshop in conjunction with Medical Image Computing and Computer Assisted Intervention (MICCAI) 2007. In this workshop, originally pathological CT scans from a variety of different CT scanners were acquired in the portal phase. Identical reference data and evaluation tools were applied for all algorithms.

Ten automatic and six interactive algorithms were evaluated, compared to each other and their results published.[3] The workshop is over, but the liver segmentation competition continues through the website (www.sliver07.org).

A comprehensive review of different techniques for liver segmentation based on CT images was done by Campadelli *et al.*,[5] describing different methods and techniques for liver segmentation along with their drawbacks.

Through MICCAI workshop comparisons and this comprehensive review, liver segmentation methods and techniques are based on live wire segmentation,[6,7] gray-level based methods,[3,8] neural networks,[9] model-fitting techniques,[4,10–18] probabilistic atlases,[14,19–22] level-set approaches,[23–25] two-dimensional region growing,[26] neighborhood-connected region-growing (NCRG),[27] and graph cut based approaches.[28–37] Some of the techniques are developed or integrated with others achieving better results when compared with their individual results.

Live-wire segmentation approaches divide the liver through a set of seed points chosen manually to determine the boundary of the liver.[6] This technique is combined with Radial bias functions and level sets to segment the liver semiautomatically,[7] achieving rank 2 (84.6) on sliver07 (April 2013). With the live-wire technique, the user has full control over the segmentation process. As a consequence, the resulting segmentation is heavily dependent on the operator's skill, potentially limiting accuracy because of possible individual errors and biases.[5]

With gray-level based methods, liver gray levels are estimated through statistical analysis of some slices segmented manually or by histogram analysis in a gray level range. An iterative threshold is applied to further create a binary volume in 2D or 3D. Morphological operations are applied to eliminate attached organs. These methods do not take into account the wide variability of CT volumes.[5]

Neural network-based methods use the gray level features corresponding to the liver for segmentation. The networks learn three patterns: liver, liver boundary, and nonliver patterns. Then, morphological operations, boundary detection by Laplacian filtering, and B-spline curves are used to refine boundaries. Those techniques are likely to fail when two neighboring organs have similar intensities.[5]

Statistical shape models (SSMs) are model-fitting techniques frequently used for segmenting the liver. In a comparative study,[3] shape-constrained segmentation methods were matched with SSMs, a technique that requires a large amount of training data to construct an SSM fitting with different liver shapes. However, SSMs are much harder to model when working with highly complex and variable shapes such as the liver.[4,5] Kainmuller *et al.*[11] automatically segmented the liver through a combination of a constrained free-form model with a statistical deformable model around the liver boundary, achieving the best score (77.3) for automatic segmentation on sliver07 website (April 2013). Wimmer *et al.*[12] proposed a probabilistic active shape model and applied it for liver segmentation achieving the second best score (76.8) for automatic segmentation on the site (April 2013).

Probabilistic atlases are constructed through the deposition of a large amount of training computed tomography (CT) data into a standard space defined by a small number of landmarks. The atlas is created by a spatial averaging of the registered organs.[5] Compared with shape models, atlas-based methods appear to have more problems in adapting to the wide variability in shape and size of livers.[3]

Level set approaches segment the liver based on a novel speed function.[5] The user has to draw rough contours inside the liver in a number of transverse slices to initialize level set evolution. This initialization employs a novel definition of the speed function. However, stopping the level set evolution based on standard terms is not reliable due to the low contrast between tissue types.[3]

Neighborhood connected region growing is used for segmenting the liver from the portal phase of a CT dataset. A liver region is initialized to be used as a seed region. From this region, the liver is segmented using NCRG. Dilation is then used to overcome undersegmentation. However, other organs of intensity similar to the liver could not be separated and low intensity tumors were undersegmented.[27]

Graph-cut approaches for liver segmentation are extensions of Boykov graph cuts.[20,21] Beichel *et al.*[22] uses the graph-cut approach as an initial segmentation of the liver followed by an interactive refinement step to overcome merged organs with liver and undersegmentation of tumors with different gray values, achieving the fourth best score (82.1) for semiautomatic segmentation on the site (April 2013) with a running time of 36 min.[3,30] Afifi *et al.*[31] integrate shape and statistical information of the liver with a graph-cuts algorithm to segment the liver semiautomatically achieving the fifth best

score (81.8) on the site (April 2013). Linguraru *et al.*[35,37] combined different techniques to segment the liver automatically. Liver is initialized based on an atlas using adaptive enhancement estimations. A fast marching level set is applied to grow the segmentation. A geodesic contour is applied to refine the segmentation result. Graph cut is applied to segment hepatic tumors. This approach achieved the third best score (76.2) for automatic segmentation on the site (April 2013) with a running time 50–60 min.[37]

The literature yields numerous examples of the various drawbacks associated with liver segmentation from the portal phase of a CT dataset. These problems include: (1) wide variability of anatomic structures of the liver in shape and size;[3,21,27,38] (2) insufficient separation on CT images of other abdominal organs of similar intensity to the liver;[1,23,24,38,39] and (3) undersegmentation of low-intensity tumors (LITs).[27,38,40–42]

Blood vessels (BVs) provide unique details for each liver in terms of organ shape and size. Therefore, we propose a method that uses abdominal blood vessel (ABV), hepatic blood vessel (HBV), and non-HBV, information to constrain liver segmentation from the portal phase of a CT dataset aiming at addressing the aforementioned issues.[43,44] Saitoh *et al.* used HBVs to segment the liver.[45] Therefore, their method is expected to take into consideration the wide variability of liver shapes and sizes. However, these authors did not clarify the capability of their method at separating liver from other neighboring organs of similar intensity and segmenting LITs.

Our proposed method differs from this approach[45] at many points: (1) for segmenting the liver core region, the proposed method applied Delaunay triangulation using end points of HBVs and intensity of CT image, not HBVs itself as used in Saitoh *et al.*, (2) for separating the liver from other organs, the proposed method uses HBVs, non-HBVs, the heart, and bones information to construct a boundary surface fitting robustly between the liver and other organs of similar intensity, not by erosion and dilation as in Saitoh *et al.*, and (3) for segmenting LITs, the proposed method fits the histogram of the core region using a variational Bayesian Gaussian mixture model, whereas in Saitoh *et al.* segmenting LITs is not mentioned at all.

We trained our method using 20 MICCAI training datasets and present the results of testing this method using 10 MICCAI-test datasets for an adequate comparison with the literature, and 50 non-MICCAI datasets from Tokushima University Hospital. The proposed segmentation technique allows volumetric information about the liver and hepatic tumors as well as HBVs vascular tree in the liver and connections with main ABVs. This information may help surgeons at planning different hepatic surgeries.

2. MATERIALS AND METHODS

The idea proposed here is to segment the liver semiautomatically based on BV information taken from only the portal phase of an abdominal CT dataset. This segmentation is achieved in two stages. First, ABVs are extracted and classified into HBVs and non-HBVs with a small number of interactions (Sec. 2.B). This extraction of BVs is just an initialization step to find the core region of the liver and some external boundaries that will drive final liver segmentation. Second, HBVs and non-HBVs are used to constrain the automatic segmentation of the liver (Sec. 2.C).

2.A. Materials

A contrast-enhanced CT scan usually consists of triphasic evaluation, including an arterial phase, a portal venous phase, and an equilibrium phase. The portal venous phase of a CT scan is acquired 50–70 s after initiation of contrast media administration, and clearly shows hepatic portal branches.[46]

The method herein uses the portal phase. In this phase, the liver parenchyma is enhanced, portal and hepatic vein enhancement is higher than the liver parenchyma, common tumors are less enhanced than liver parenchyma, some tumors are more enhanced than the aorta,[47] kidneys, renal arteries, and veins are enhanced, the aorta is still enhanced, the inferior vena cava (IVC) is slightly enhanced, and the heart is enhanced. These characteristics of the portal phase may vary according to the time that the portal phase is achieved. In the late portal phase, the renal parenchyma has almost the same contrast as liver.

MICCAI training data (20 datasets) are used for training and setting different variables in the proposed method. Then, the performance of the method is tested using two databases: the MICCAI-test database (10 datasets) and the non-MICCAI database (50 datasets). MICCAI data (training and test) and reference labeling of training datasets were downloaded from the sliver07 website. All MICCAI datasets were enhanced with contrast agent and scanned in the central venous phase on a variety of scanners (different manufactures, 4, 16, and 64 detector rows). All datasets were acquired in the transversal direction. Pixel size spacing varied between 0.55 and 0.80 mm, the interslice distance varied from 1 to 3 mm. Most of these datasets were pathologic and included tumors, metastases and cysts of different sizes.[3,48] To generate reference segmentation for MICCAI data, radiological experts manually outlined liver contours for all datasets in the transverse plane in a slice-by-slice fashion.[3] Non-MICCAI data are 50 contrast-enhanced multislice abdominal CT datasets at the portal phase from Tokushima University Hospital, Tokushima, Japan. These data contain 20 normal and 30 abnormal datasets and collected following national privacy laws. Abnormal datasets contain 45 tumors of different sizes [average maximum length, 38.2 mm; standard deviation (SD), 21.1 mm], with 13 tumors adjoined to the liver boundary and 32 located inside the liver. These datasets were acquired using a Toshiba Aquilion scanner (Toshiba Medical Systems, Otawara-shi, Tochigi, Japan; tube current: 100–360 mA; tube voltage: 120 kV; reconstruction functions: FC01, FC13; one scan time: 0.5 s). Slice thickness was 1 mm. Each slice had a size of 512 × 512 pixels, and pixel size ranged from 0.546 to 0.683 mm. The 3D coordinate system had the Z-axis parallel to the body axis and oriented from the topmost to the bottommost slice. X- and Y-axes were oriented along the width from right to left and the height from bottom

to top of the axial slice, respectively. MICCAI training and test data have one reference for each dataset. We obtained one reference for each dataset of non-MICCAI data as well. For obtaining this reference, two experts with five years experience in CT image analysis segmented livers in these datasets. Each expert was assigned 25 datasets to segment the liver manually in the transverse plane in a slice-by-slice fashion. Segmentation results of each expert are checked by the other. When there was a disagreement about a liver contour at any region, the two experts discussed and corrected the liver contour at the variability region. The final results were one reference data for each dataset. This reference is used for evaluation of the non-MICCAI data.

2.B. Extraction of ABVs and subsequent classification into HBVs and non-HBVs

2.B.1. Extraction of ABVs

Extraction of ABVs from CT images is achieved in three steps: (1) removal of bone, accumulated calcium, and kidneys; (2) enhancement of peripheral BVs; and (3) extraction of ABVs.

2.B.1.a. Step 1: Removal of bone, accumulated calcium, and kidneys. Image noise is reduced using a median filter [Fig. 1(a)].[49] A review of the MICCAI training data revealed that ABVs and the liver (e.g., liver and tumor tissues) are in the range of 0–350 Hounsfield units (HU). Bone and accumulated calcium (if any) are extracted by applying a threshold technique with a value greater than 350 HU. Labels of volume < 1 mm^3 are deleted from the threshold result. Kidneys are extracted using seeded region-growing (SRG).[50] The user chooses manually a seed point at a high intensity region of the renal cortex of the right kidney. Automatically, this seed point is replaced by a 2D-region centered at the seed point with a radius of 2 mm. The mean intensity (HU) of points in this region is obtained. The region grows connecting points with intensity more than or equal to this mean. The volumetry of this region growing result (V_1) is measured. Next, region growing is repeated with intensity 3 HU lower than the first mean. This process is repeated iteratively, decreasing the mean each time by 3 HU. The volumetry of each region growing result (V_i) is measured. The difference in volume between two consecutive iterations is measured as well. The region growing stops when $(V_i - V_{i-1})/V_{i-1} \geq 0.2$, and $V_{i-1} > 0$ where $i = 2, 3, 4$, etc. The value 0.2 is chosen experimentally based on a review of MICCAI-training data to avoid region growing leakage into neighboring organs. The left kidney is extracted in the same method. In late portal phase case, the region growing for extracting kidneys may leak into the liver through the vena cava. The user corrects this leakage by first deleting manually the label of a slice of the vena cava between the right renal vein and the liver, and second applying an erosion operation of radius 1 mm to the result and selecting the region that is connected with the seed point of the right kidney. A dilation of 1 mm followed by a closing operation[51] of 2 mm is applied to the extracted regions to cover bone, accumulated calcium (if any), and kidneys [Fig. 1(b)]. Through changing the CT value at the closing result into a negative value, bone, accumulated calcium, and kidneys are removed [Fig. 1(c)]. Changing into a negative value results in a high level of variation in the intensity between the liver and these extracted regions. This variance in intensity prevents leaking of the liver into these regions during the liver-core-region extension process described in Sec. 2.C.

2.B.1.b. Step 2: Enhancement of peripheral BVs by two grayscale morphological operations. Anatomically, peripheral BVs and tissues have very small differences in intensity. To emphasize peripheral BVs, an opening in 3D is applied at regions > 0 HU. In this opening, two morphological operations (i.e., erosion and dilation) are applied consecutively with three radii with lengths of 1, 2, and 4 voxels. When the radius is equal to one voxel, the erosion operation requires that the central voxel takes the minimum value of its 3D surrounding voxels. At the dilation operation, the central voxel takes the maximum value among its own value and the values of its surrounding voxels. The result of this step is used as an input to the next. The operations diverge when the radius is less than or equal to two voxels: for erosion, all of the inside voxels take the minimum value of their outer boundary voxels, whereas for dilation, the inside voxels take the maximum value of their own values and the values of their surrounding voxels. The image that results from this corrective action can then be applied when the radius is ≤ 4 voxels (3 mm). This process obtains a blurred image (background) fitting adequately with tissues and BVs of radii > 3 mm.

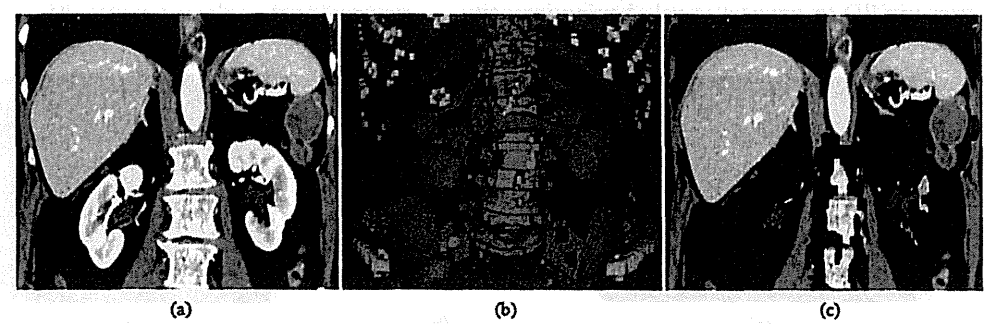

FIG. 1. Removal of bone, accumulated calcium, and kidneys. (a) Noise of original image is reduced using a median filter. (b) Bone and accumulated calcium are extracted through a threshold. Kidneys are extracted using a seeded region-growing. (c) Extracted regions are removed. Accumulated calcium is marked by an arrow.

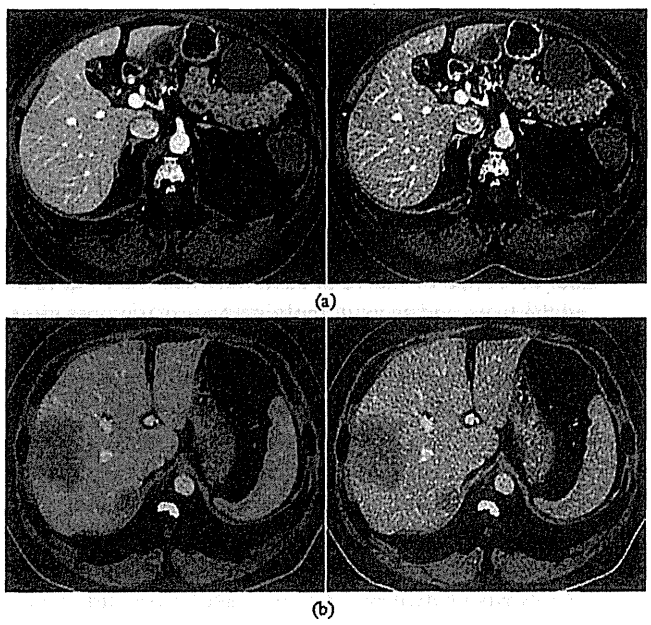

FIG. 2. Enhancement of peripheral blood vessels is achieved using 3D bias field correction. (Left) CT image before enhancement and (right) after enhancement. (a) A nonlow intensity tumor (NLIT) case (MICCAI-training-15) and (b) a LIT case (MICCAI-training-16).

By subtracting this background from the image that ensues from removal of bone, accumulated calcium, and the kidneys [Fig. 2(a, left)], peripheral BVs remain. These remaining peripheral BVs are added to the image in Fig. 2(a, left) enhancing peripheral BVs [Fig. 2(a, right)]. In LIT cases [Fig. 2(b)], this enhancement increases the extracted peripheral blood vessels that surrounds low intensity tumors in three dimensions.

2.B.1.c. Step 3: Extraction of ABVs. Using the enhanced BVs CT image (only at this step), a 3D seeded region growing technique is performed to extract ABVs. An axial section containing the entrance of the IVC is selected manually. The seed point is initialized manually at the entrance of the IVC [Fig. 3(a)]. To avoid any potential interuser variability in choosing the seed point, a 2D region centered at the chosen seed point with a radius of 6 mm is selected automatically. A histogram of this region is calculated. A threshold is set at the 75th percentile HU of the histogram [Fig. 3(b)]. Points in the selected region with intensity more than or equal to this threshold are the actual seed region for the region growing. This region grows in 3D to connect voxels having intensity more than or equal to the threshold. Volumetry of this region growing result (V_1) is measured. Next, the seed region grows connecting voxels with intensity 3 HU less than the threshold. This process is repeated iteratively, decreasing the intensity each time by 3 HU. The volumetry of each region growing result (V_i) is measured. The region growing stops when $((V_i - V_{i-1})/V_{i-1}) \geq 0.2$ and $V_{i-1} > 0$, where i = 2, 3, 4, etc.

ABVs of the majority of abdominal organs are extracted through this region growing [Fig. 3(c)]. A section of the heart is extracted with ABVs owing to its similarity in intensity with ABVs in the portal phase. In diseased cases, hepatic tumors with intensity close to ABVs (or high-intensity tumors) are also extracted. Extraction of a section of the heart and hepatic tumors with ABVs do not affect liver segmentation, as the hepatic tumors are reduced into points inside the liver when constructing the liver core region (Sec. 2.C), and as the extracted heart sections are classified as non-HBVs.

2.B.2. Classifying ABVs into HBVs and non-HBVs

Extracted BVs are classified into HBVs and non-HBVs in three steps: (1) removal of main BVs, proper hepatic artery, the heart, and high-intensity tumors; (2) clustering of medial and peripheral BVs; and (3) classification of HBVs and non-HBVs.

2.B.2.a. Step 1: Removal of main BVs, proper hepatic artery, the heart, and high-intensity tumors. ABVs and part of the heart are classified into different categories by assigning each voxel of the segmented vessel and heart a specific value. This value is decided according to the thickness of the vessel and heart component containing this voxel. This procedure was performed using a reverse-squared Euclidean distance transformation parallel type algorithm[52] [Fig. 4(a)]. These categories are assigned numbers in an ascending order from thinnest to thickest. For removing main connections between HBVs and non-HBVs, the user selects manually the number of the category associated with the thickest part of the main portal vein (the entrance of the portal vein to the liver). Deleting this category disconnects the entrance of the PV to the hepatic PV. However the proper hepatic artery will be still connecting the abdominal aorta and HBVs because it is thinner than the entrance of the PV. To disconnect the proper hepatic artery, main BVs that are assigned numbers greater than or equal to the selected number [Fig. 4(b)], are 3D-dilated by

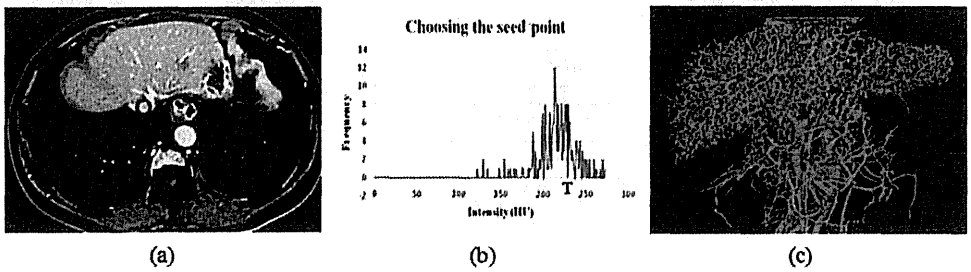

FIG. 3. Extraction of ABV: (a) an enhanced image (entrance of the inferior vena cava is marked with a circle), (b) 2D histogram of the region inside this circle (threshold value is marked with (T) which represents 75th percentile), and (c) extraction result.

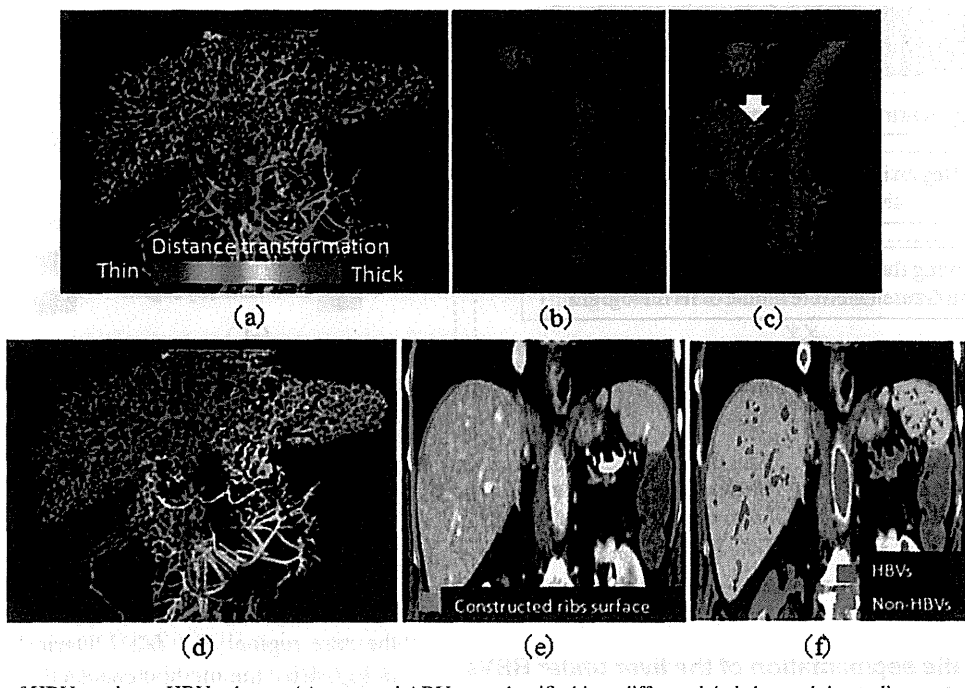

FIG. 4. Classification of HBVs and non-HBVs cluster: (a) extracted ABVs are classified into different labels by applying a distance transformation technique. (b) Main BV and parts of the heart are selected for dilation. (c) BVs of (a) that included at the region of dilating (b) are separated (proper hepatic artery is marked with an arrow). (d) Remaining BVs and parts of the heart are classified into different clusters. (e) Extracted ribs boundary surface and (f) HBVs and non-HBVs cluster are classified (ribs boundary surface, eroded main BV, the right kidney, the heart and accumulated calcium (if any) are added to the non-HBVs cluster).

10 mm. The result in Fig. 4(a) is overlapped with this dilation region. In the dilation region, main portal vein, proper hepatic artery, the entrance and exit of the IVC to the liver, the abdominal aorta, parts of the heart, and any extracted large high-intensity tumors (if any) are extracted [Fig. 4(c)]. The region in Fig. 4(c) is removed from the extracted BVs in Fig. 4(a), as shown in Fig. 4(d) resulting in removal of main connections of HBVs with non-HBV. In some cases, entrance or exit of the IVC to the liver is not separated from HBVs by this interaction. This is corrected through manually deleting the label of the IVC in two slices: one between HBVs and the heart and the other at the exit of the IVC from the liver.

2.B.2.b. Step 2: Clustering medial and peripheral BVs. By using the remaining vessels after separation of main BVs, medial and peripheral BVs are then classified into different categories in an ascending order from the thinnest to the thickest as we aforementioned. BVs with the first-order category are classified as peripheral BVs, where all other remaining BVs are classified as medial BVs. Peripheral BVs are separated from medial ones. Consequently, medial BVs of different organs become disconnected from each other. Through assigning a label to each connected group of BVs, medial BVs are obtained in different labels. Each label represents one cluster of medial BVs. Through checking connectivity of each peripheral BV with its neighboring clusters of medial BVs, peripheral BVs are classified into two clusters. The first cluster includes peripheral BVs that are connected to only one cluster of medial BVs. The second includes peripheral BVs that are connected into two or more of medial BVs clusters. The second cluster of peripheral BVs is deleted completely to avoid connections between medial BVs clusters. The first cluster of peripheral BVs is added back to medial BVs clusters. In this way, clusters of medial and peripheral BVs of different organs are obtained [Fig. 4(d)].

2.B.2.c. Step 3: Classification of HBVs and non-HBVs. The liver is the largest abdominal organ and is located at the upper-right quadrant of the abdomen.[27,32] Based on this observation, HBVs are identified and assigned to the first cluster. To determine the largest abdominal organ, volumetries of medial and peripheral BVs clusters are calculated and arranged in descending order. To determine the upper-right quadrant of the abdomen, the center of gravity of each cluster is calculated. The center of a cluster is the average a_x and a_y of X- and Y-components of all voxels included in this cluster, respectively. A cluster is classified as HBVs when it satisfies two conditions simultaneously: it has the greatest volume and its center exists at the region where $a_x - a_y \leq 0$. This cluster is assigned to the first label. All other clusters are assigned to the second label forming the non-HBV cluster. The region in Fig. 4(c) is eroded 2 mm in 3D and added to the non-HBV cluster as well. This erosion keeps main BVs disconnected from HBVs. Bones are used to construct the ribs surface. Using extracted bones, the ribs are extracted.[53] A closing operation of radius 2 mm is applied to the extracted ribs. A technique based on a two-pass thinning algorithm[49] is applied to extract the ribs center lines. The ribs boundary surface is constructed through applying Delaunay triangulation[54] to connect the thinning results with a maximum length 50 mm [Fig. 4(e)]. This length is chosen experimentally to connect different ribs and minimize connection between parts of the same rib. This surface is added to the non-HBV cluster. Right kidney and accumulated calcium (if any) are added to the non-HBV cluster as well [Fig. 4(f)].

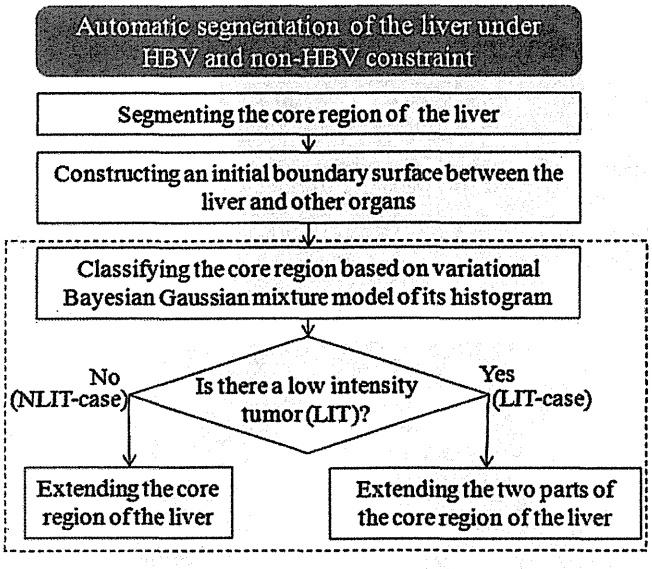

FIG. 5. Schematic diagram of the second stage of the proposed method.

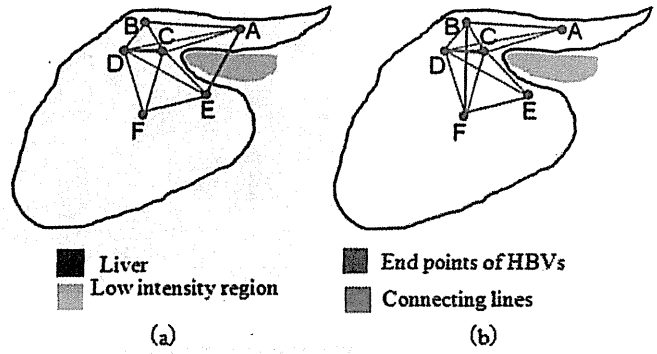

FIG. 6. Delaunay triangulation is performed based on HBV and intensity information simultaneously in the proposed method. (a) A sketch explains Delaunay triangulation when it is applied based on HBV end points only. (b) When this triangulation is applied based on HBV end points and image intensity simultaneously.

2.C. Automatic segmentation of the liver under HBVs and non-HBVs constraint

Classified HBVs and non-HBVs are used for automatic segmentation of the liver, with the subsequent image resulting from the extraction of bone, accumulated calcium, and kidneys. This process involves fours steps, as described in Fig. 5.

2.C.1. Step 1: Segmenting the core region of the liver

Using the extracted HBVs, a technique based on a two-pass thinning algorithm[49] is applied for extracting center lines of HBVs. End points of HBVs are extracted from this thinning result.[55] Delaunay triangulation[54] is applied to construct a polyhedron structure of the core region of the liver. When this triangulation is constructed based on end points only, end points are connected to each other through lines regardless of positions of these lines in or outside the liver [Fig. 6(a)]. This way of connection may cause segmentation of other organs like the gallbladder. Delaunay triangulation is developed to be applied based on HBV end points and the image (resulting from bone, accumulated calcium, and kidneys removal) intensity on the lines connecting them simultaneously. During this process, the intensity on a line is checked to determine whether it is >20 HU. When this condition is satisfied for all lines of a polygon, this polygon is constructed as a unit of the core region [Fig. 6(b)]. During the construction of ABC in Fig. 6(b), the method checks the intensity of the CT image on the lines connecting the points A, B, and C. Because all of these lines satisfy the condition, ACB will be constructed as a unit of the triangulation. However, the line AE does not satisfy the intensity condition because it passes through a lower intensity region such as the gallbladder or stomach. Therefore, the ACE will not be constructed. All other triangles having the line AE as a side will not be constructed as well. In this way, the proposed method avoids segmentation of regions outside the liver. The value of 20 HU is chosen experimentally based on MICCAI-training data to distinguish between intensities of the gallbladder and LIT. Figure 7 provides an example illustration of such a polyhedron structure of the liver core region.

2.C.2. Step 2: Constructing an initial boundary surface between the liver and other organs

To separate the liver from other organs on CT images, a boundary surface is constructed between the liver and these organs based on the segmented core region and the non-HBV cluster. This surface serves as a boundary between the liver and the neighboring organs at homogenous regions. This boundary surface is perpendicularly and equidistantly constructed in three dimensions between the core region and

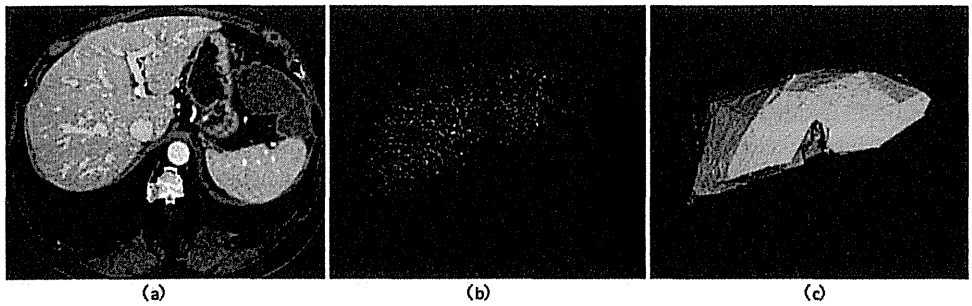

FIG. 7. Example of constructing the polyhedron structure of a liver core region using HBVs and intensity: (a) preprocessed CT dataset (without enhancement) and extracted HBVs, (b) extracted end points of HBVs, and (c) constructed polyhedron structure of the core region.

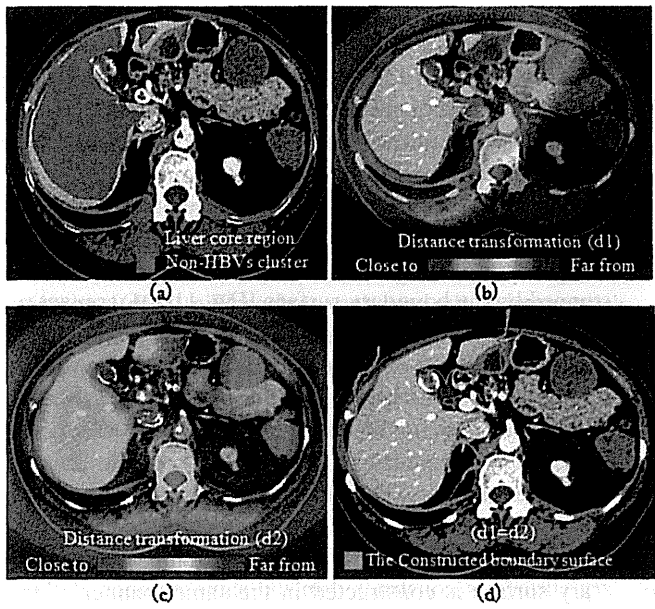

FIG. 8. Boundary surface between the liver and other organs is constructed to separate them when they have similar intensity. (a) Liver core region, non-HBVs cluster are used for constructing this surface (extracted accumulated calcium is marked with arrows). (b) Distance transformation technique is applied starting from the core region to calculate d1. (c) Same technique starting from non-HBVs cluster is applied to calculate d2. (d) The initial boundary surface is constructed at d1 = d2.

the non-HBV cluster. Starting from the core region, a distance transformation technique[52] based on Euclidian distance is used to calculate d1 (p, q), where p and q are two points of three dimensions, p on the surface of the core region and q a point external to the core region. Using the non-HBV cluster only, the same technique is employed to calculate d2 (r, s), where r is a point on the surface of the non-HBVs and s is a point external to the non-HBVs. At places where |d1 − d2| = 0, a perpendicular surface is constructed to separate the two regions. This surface is the initial boundary surface that we construct between the liver and the neighboring organs (Fig. 8).

2.C.3. Step 3: Segmenting LITs

LITs are segmented in two steps: (1) classifying the core region based on its histogram and (2) extending the core region.

2.C.3.a. Step 3.1: Classifying the core region based on its histogram. HBVs and extracted high intensity tumors are removed from the core region. The histogram of the liver core region is calculated. By fitting the histogram using a variational Bayesian Gaussian mixture model.[56] The variational Bayesian inference allows the automatic determination of the number of components in the mixture. The core region is classified based on the number of components of the mixture. When the mixture has one component, a core region is classified as a non-LIT case (NLIT-case). Meanwhile, when the mixture has two components, the core region is classified as a LIT case (LIT-case). LIT-case is classified by dividing the mixture components into two parts: NLIT- and LIT-parts. Figure 9 illustrates the classification of NLIT- and LIT-case core regions.

2.C.3.b. Step 3.2: Extending the core region. To identify the boundary of the liver on CT images, extension is done based on available intensity and the constructed boundary surface. Intensity is employed for extending the core region by

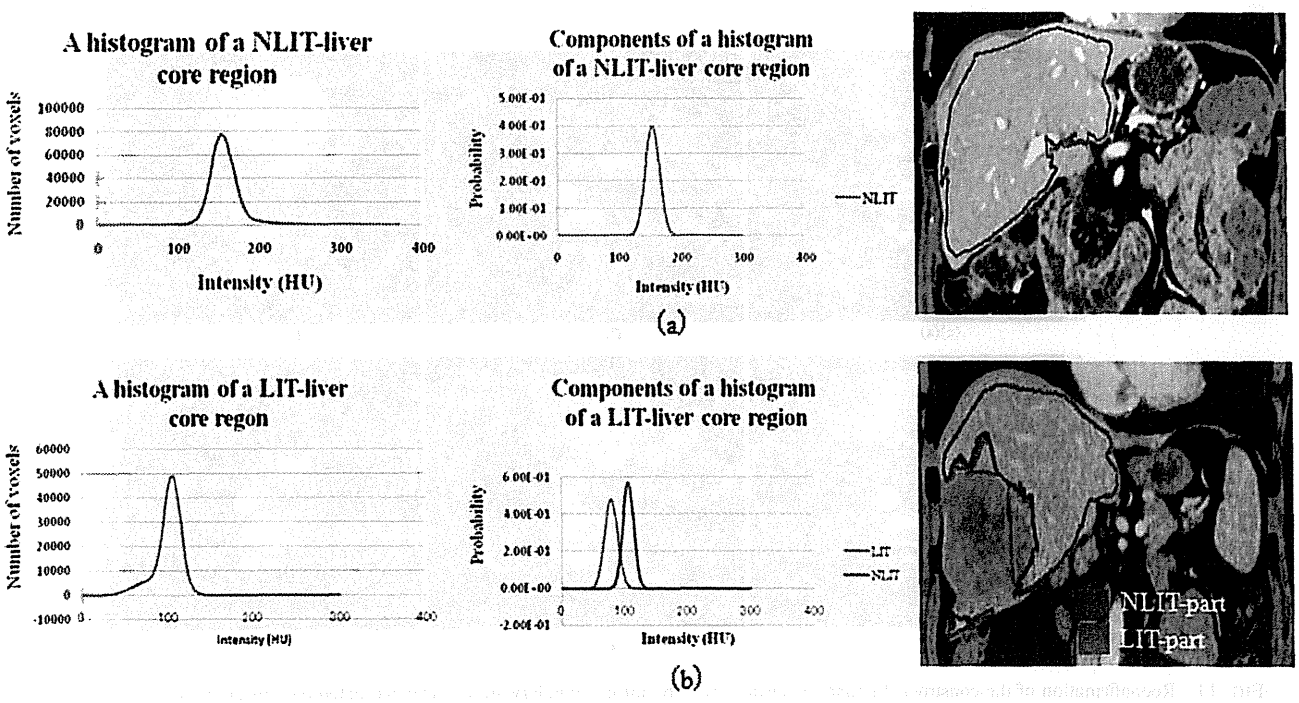

FIG. 9. Two examples of NLIT- and LIT-core regions are classified by fitting their histograms. (Left) Histograms of core regions, (middle) extracted components of each histogram, and (right) core regions are classified into NLIT- and LIT-parts based on their histograms. (a) NLIT-liver (MICCAI-training-15) and (b) LIT-liver (MICCAI-training-16).

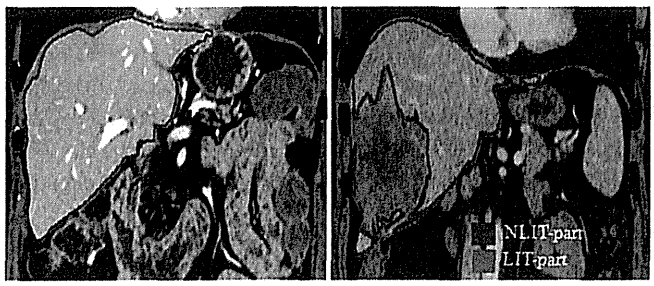

FIG. 10. Extension of liver core regions: (a) extension result of a NLIT-case (MICCAI-training-15) and (b) results of a LIT-case, the NLIT- and LIT-parts are segmented separately (MICCAI-training-16).

using the histogram to check the homogeneity of the neighboring regions by checking each voxel. The boundary surface is constructed to separate the liver from neighboring organs when they are similar in intensity.

Extension is achieved via two methods. First, for a core region of a NLIT-case, extension is done based on a single component of the histogram. The component peak is detected. Two thresholds corresponding to 10% of the height of this peak from both sides are selected for this purpose. The core region grows checking neighboring voxels iteratively; when intensities of these neighboring voxels are included in the extension range, these voxels are classified as liver candidates [Fig. 10(a)]. Second, for extending the core region of a LIT-case, the core region is classified into NLIT-and LIT-parts with two corresponding components. Each part of the core region is extended separately using the corresponding component in a similar manner to the extension of the NLIT-case. The NLIT-core region is extended, followed by extension of the LIT [Fig. 10(b)]. NLIT-extension is automatically stopped either when it reaches a variation in intensity between the liver and neighboring regions or when it reaches the boundary surface. Extension of LIT is automatically stopped either when it reaches a variation in intensity or the boundary surface or the extension result of the NLIT-part. HBVs and segmented hepatic tumors are added to the extension result.

In some regions where BVs are not extracted properly, the initial boundary surface intersects the liver causing under-segmentation [Fig. 11(a)]. Therefore when the extension is stopped by the boundary surface [Fig. 11(b)], contact regions between the extension result and this surface are reconfirmed to distinguish between the liver and neighboring organs. A voxel on the initial boundary surface is classified as a voxel of a contact region when one of its 26 neighbors is a voxel of the extension result [Fig. 11(c)]. Contact regions are assigned to different labels. A contact region "a_0" is measured through multiplying number of voxels that is included in this region by the voxel volume. When $a_0 \geq 50$ mm^3, a second boundary surface is constructed in the same manner of the initial boundary surface [Sec. 2.C.2 (Step 2)] using the extension result (instead of the core region) and the non-HBVs cluster [Fig. 11(d)]. The value 50 mm^3 was chosen experimentally to exclude small contact regions from re-extension. The contact region grows checking neighboring voxels iteratively with the second extension range; when intensities of these neighboring voxels are included in the second extension range, these voxels are classified in the extension result [Fig. 11(e)]. This region growing is restricted between the initial and the second boundary surfaces. The second extension range is obtained based on the histogram of the core region and its extension result in the same manner of the first extension range. Contact region [a_1] between first contact region extension and the second boundary surface is obtained. The volume of the first

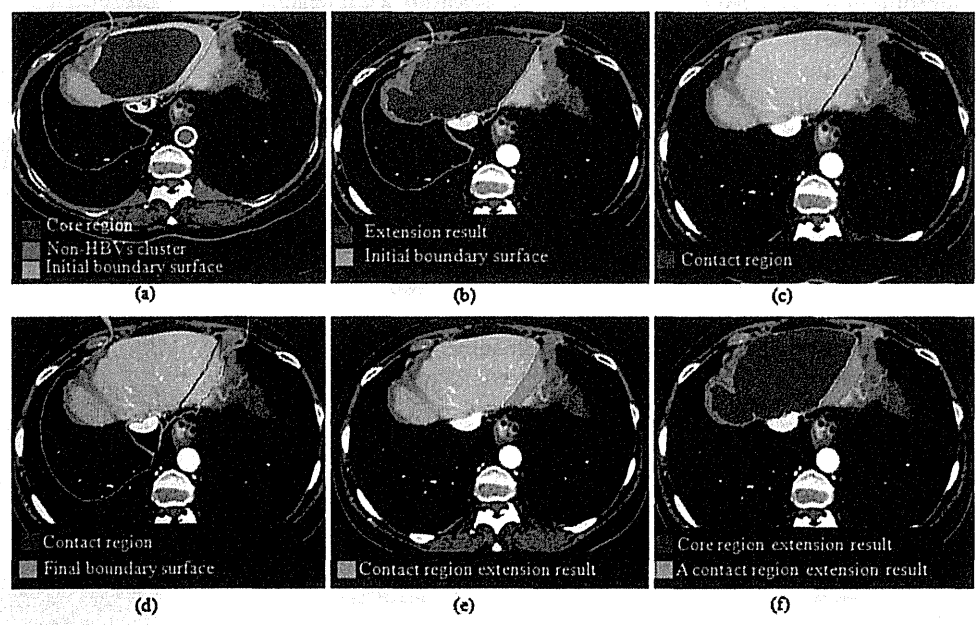

FIG. 11. Reconfirmation of the constructed boundary surface. (a) The initial boundary surface is constructed equidistantly between the core region and non-HBVs cluster. (b) Extension result and the initial boundary surface are used to identify their contact region. (c) Contact region is illustrated. (d) Final boundary surface is constructed between the extension results and non-HBVs cluster. (e) A contact region extension result, and (f) contact region extension result is added to the first extension.

contact region extension [v_1] is measured through multiplying the number of voxels that is included in this extension by a voxel volume. This process is repeated iteratively and "a_i" and "v_i" are measured where i = 2, 3, 4, etc. This iteration is automatically stopped when at least one of the following conditions is satisfied in the same priority mentioned here: (1) when $a_i < 50$ mm^3, (2) when $v_i < 300$ mm^3, and (3) when $a_i \geq a_{i-1}$ and $a_{i-1} > 0$ (a local minimum of a_i is detected). The value "300 mm^3" was chosen experimentally to stop iteration before leakage into neighboring organs.

Other contact regions are re-extended in the same manner and added to the core region extension result. The results of one contact region and the core region extensions are illustrated [Fig. 11(f)].

2.C.4. Step 4: Refining the segmented liver

Refining the segmented liver is performed in two steps: (1) refining main BVs using a solid angle and (2) filling holes in 3D.

2.C.4.a. Refining main BVs using a solid angle. During classification of BVs of different organs (Sec. 2.B.2), some parts of main BVs are misclassified at the liver entrance, causing under- or oversegmentation. These BVs are refined as follows:

Each voxel of the segmented liver is checked with its 26 neighbors. When one or more of these neighbors is not a liver, this voxel is considered as a liver surface candidate. When these neighbors are included in main BVs, they are considered as intersecting voxels of liver with main BVs. Starting from each voxel of this intersection (X, Y, Z) as a center, a rectangular box of length 30 mm, width 30 mm, and height 30 mm is selected. Main BVs within this region are selected for classification using a solid angle [Fig. 12(a)]. A solid angle with a vertex at a voxel p of main BVs is defined as follows:[57]

A solid angle = Count 2/Count 1,

where "Count 1" represents the total number of vectors that are generated with equivalent angles from p to all voxels of the surface of a sphere centered at this voxel. "Count 2" represents the number of vectors that pass through the same sphere and intersect the segmented liver surface. The maximum checking region for intersection of these vectors with liver tissue is set to the surface of a sphere centered at p with a radius $r = 15$ mm. This radius is chosen experimentally to exclude the region of the liver surface marked with arrows [Fig. 12(a)] when calculating the solid angle (Count 2). When this solid angle is ≥ 0.5, the voxel p is classified as a voxel of HBVs and added to the segmented liver [Fig. 12(b)].

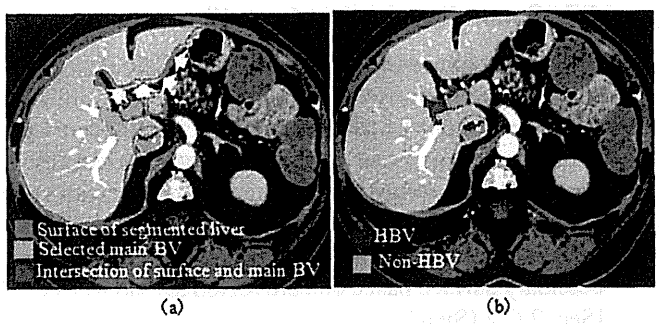

FIG. 12. Refining main BV based on solid angle: (a) an example of the selected region of main BVs (liver surface at the region that is marked with arrows is excluded when calculating solid angles by setting r = 15 mm) and (b) main BV at the selected region are classified into HBVs and non-HBVs (MICCAI-training-15).

2.C.4.b. Filling holes in 3D. Holes are filled in 3D to avoid undersegmentation. In this step, when a hole is surrounded by NLIT, it is filled and added to the NLIT. Whereas, when the hole is surrounded by an LIT, it is filled and added to the LIT. Holes that are surrounded by LIT and NLIT are filled and added to the NLIT (liver). To smooth the surface of the segmented liver, an opening operation is applied with a radius of 1 mm.

3. RESULTS

MICCAI-test and non-MICCAI databases are used to evaluate the precision of the proposed method. Segmented livers were compared with their corresponding references. Five measures of accuracy from the MICCAI workshop for liver segmentation in 2007 were applied for all segmentation results. These measures are based on volumetric overlap and surface distances, and calculated as in Heimann *et al.*[3] These measures are volumetric overlap error (VOE), relative volume difference (RVD), average symmetric surface distance (ASD), root mean square symmetric distance (RMSD), and maximum symmetric surface distance (MSD). Segmentation is perfect (worth 100 per measure) when each of these measures is zero. The RVD is given as a signed number to show if the method tends to under- or oversegment. In addition to the MICCAI measures, the following volume measures[27] were applied for the non-MICCAI datasets:

- TPVT, in percent = (number of true positive in the segmented image/number of voxels in the liver's reference) $\times$ 100.
- FPVT, in percent = (number of false positive voxels in the segmented image/number of voxels in the liver's reference) $\times$100.

Evaluation of MICCAI test data was performed by the organizers of the sliver07 website. These organizers applied the same tools and scoring system that they used in the MICCAI workshop for liver segmentation in 2007, and this tool calculates the same five measures as sliver07. These results are summarized in Table I with an overall score of 85.7, which ranks best among results on the site as of July 2013.

The precision of the method was also evaluated by applying the same measures and other standard measures to the results obtained from non-MICCAI data, as illustrated in Table II. Tables I and II demonstrate the usefulness of the proposed method at segmenting livers form MICCAI and non-MICCAI databases.

Our study found the processing time (average $\pm$ SD) for extracting and classification of BVs to be 4.6 $\pm$ 0.9 min when applied by an experienced user. The user with low experience may need one minute more for correction of

TABLE I. Evaluation of the method performance based on MICCAI test data results was obtained by the organizers of sliver07 website using the same tools and scoring system that were used in the 2007 MICCAI workshop (SD: standard deviation).

Measure	VOE		RVD		ASD		RMSD		MSD		
Test case	(%)	Score	(%)	Score	(mm)	Score	(mm)	Score	(mm)	Score	Total score
1	4.3	83.2	1.02	94.6	0.58	85.6	1.02	85.8	10.12	86.7	87.2
2	4.19	83.6	-0.78	95.9	0.58	85.4	1.36	81	17.62	76.8	84.6
3	4.28	83.3	1.16	93.9	0.8	79.9	1.27	82.4	17.65	76.8	83.2
4	4.72	81.6	−0.3	98.4	0.68	83	1.38	80.8	15.4	79.7	84.7
5	5.33	79.2	−0.26	98.6	0.87	78.3	1.55	78.4	15.88	79.1	82.7
6	3.81	85.1	−0.67	96.4	0.54	86.5	1.07	85.1	11.99	84.2	87.5
7	3.11	87.9	0.41	97.8	0.41	89.8	0.84	88.3	9.43	87.6	90.3
8	4.53	82.3	0.91	95.1	0.69	82.7	1.38	80.9	15.24	79.9	84.2
9	3.6	85.9	1.68	91	0.39	90.2	0.66	90.8	13.02	82.9	88.2
10	5.46	78.7	−0.35	98.1	0.73	81.8	1.32	81.6	13.7	82	84.4
Average	4.33	83.1	0.28	96	0.63	84.3	1.19	83.5	14.01	81.6	85.7
SD	0.73	2.84	0.87	2.42	0.16	3.93	0.28	3.88	2.88	3.79	2.46

interactions' results. The time for segmenting the liver stage was 6.8 ± 1.7 min; here, studied cases had 232 ± 114.6 slices. This was observed when applying the proposed method using a standard computer (Dell Precision T3500, 2.67 GHz Intel Xeon® W3520 CPU, 6.00 GB RAM, Windows Vista™ Business operating system). Processing time can be further decreased through the use of multithread processing.

A visual comparison between segmented livers and their corresponding reference data is shown in Fig. 13.

A review of the proposed method performance on healthy and unhealthy cases of both MICCAI-test and non-MICCAI data are presented in Table III. In order to verify the hypotheses that the method performance does not defer when applied to different datasets, p-values (p) from a nonparametric test[58] (Wilcoxon-Mann-Whitney rank sum test) are calculated based on the MICCAI-test and non-MICCAI data for the five measures of evaluation and are presented in Table IV. Through Tables III and IV, it can be noticed that there is no significant difference ($p > 0.05$) between the performances of the method when applied to healthy and unhealthy datasets. Whereas, the results that were obtained based on non-MICCAI data are significantly ($p < 0.05$) more accurate than the corresponding results that were obtained based on MICCAI-test data. MICCAI-data were scanned using a variety of scanners and scanning conditions[3,48] whereas non-MICCAI data were scanned using the same scanner with a relatively high resolution. The use of newer CT scanners is expected to result in higher-resolution images; consequently, the performance outcomes of the proposed method are expected to be much higher with recent CT scanners than the scanners used in this study.

TABLE II. Evaluation of the method performance using 50 non-MICCAI datasets according to MICCAI workshop measures and other standard measures. Results represent average and standard deviation (SD) of the overall data. Measures are calculated as in Ref. 3.

Measure (unit)	TPVF (%)	FPVF (%)	VOE (%)	RVD (%)	ASD (mm)	RMSD (mm)	MSD (mm)
Average	97.56	1.35	3.21	0.06	0.45	0.98	12.69
SD	1.05	0.82	0.75	1.29	0.17	0.26	3.89

4. DISCUSSION

4.A. Addressing the wide variability in liver shapes and sizes

Our proposed method is based on BV anatomy, which is unique to each scanned liver because of the considerable shape and size variability of livers; this method is thus quite valuable for addressing this wide variability in liver anatomy. In Table V, the average volume over all reference datasets is 1 281 132 mm^3, with an SD of 645 925. This large SD reflects the wide variability of the sizes of livers used in this study. The utility of the proposed method for addressing this variability is reflected in the strong correlation [correlation coefficient (CC) = 0.9988] between reference and segmented livers overall, using the MICCAI training as well as non-MICCAI data [Fig. 14(a)]. This capability is also reflected in the strong correlation (CC = 0.9995) between liver reference and overlapping regions [Fig. 14(b)].

4.B. Separating the liver from other organs

In several approaches (Refs. 23, 24, 27, 38, 39, and 41) for segmenting the liver from the portal phase of a CT dataset, the liver could not be separated from its neighboring organs of similar intensity. Our proposed method successfully segments the liver without interference from other nearby organs. This is achieved based on (1) variation in intensity between the liver and its neighboring organs and (2) constructing a boundary surface based on core region and non-HBVs cluster [Sec. 2.C.2 (Step 2)].

Variation in intensity is applied by using the range of extension that is decided based on the components of the core region histogram. This core region intensity is higher when compared with neighboring organs such as the gallbladder,

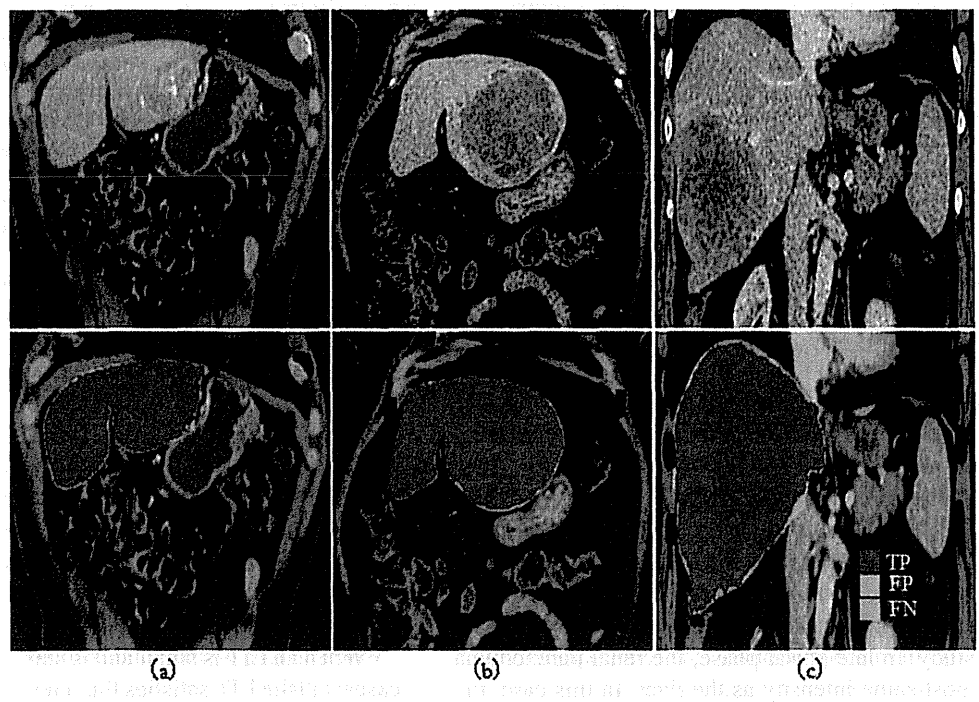

FIG. 13. Evaluation of segmented livers on scans containing severe pathological abnormalities. Although abnormalities, segmented livers agree with their references. (a) Large tumor with high intensity, (b) large LIT (non-MICCAI data), (c) large LIT (MICCAI training 16). (Up) Original dataset and (down) results of overlapping both segmented livers and their references are illustrated.

the stomach, surrounding muscles, air regions, etc. Bones are also separated based on variation in intensity with the liver where their intensity is changed into a negative value [Sec. 2.B.1 (Step 1)]. This variation stops segmentation of the liver from leaking into these organs during the extension process. The boundary surface prevents the liver from leaking into neighboring organs having a similar intensity when they are overlaid close to each other during extension of the core region such as the kidneys, the spleen, the heart, the pancreas, the intestines [Figs. 15(a) and 15(b)], and muscles at LIT-cases. As an example, the stomach is usually separated through variation in intensity with liver tissue. However, in the abnormal stomach (i.e., one having high intensity and located overly close to the liver), the stomach is extracted and classified in the non-HBV cluster. The boundary surface then prevents leakage of the liver into the stomach on CT images [Fig. 15(c)].

The gallbladder sits just beneath the liver and has an intensity that is lower than the liver parenchyma, HBVs and mostly LITs. The gallbladder is excluded from the liver core region by applying the intensity condition of Delaunay triangulation [Sec. 2.C.1 (Step 1)]. It is also excluded during extension of the liver based on intensity variation of histogram components. In LIT-livers, the NLIT-core region is extended first and stops from leaking into the gallbladder based on intensity variations as usual, then this extension result is used to stop LIT-core region extension from leaking into the gallbladder. In some abnormal cases, the gallbladder contains some accumulated calcium. This calcium is extracted with bone and added to the non-HBV cluster [Sec. 2.B.2.c (Step 3)]. Consequently, the boundary surface prevents leakage into the gallbladder [Figs. 8(a) and 8(d)]. This boundary surface is a salient feature of the proposed method.

Muscles are usually separated based on intensity variation with the liver parenchyma. In LIT-cases, muscles have nearly the same intensity of LIT and overlay close to each other [Fig. 16(e)]. Therefore, Muscles are separated from LIT by the constructed boundary surface. To construct this boundary surface, the ribs boundary surface [Sec. 2.B.2.c (Step 3)] is added to the non-HBVs cluster to set the boundary surface inside ribs cage. This ribs boundary surface could effectively solve the problem of separating muscles form the LITs neighboring the ribs cage. Muscles on the inner surface of the liver are separated from neighboring LITs by the boundary surface.

TABLE III. Comparison of the performance of the proposed method based on healthy and unhealthy cases of MICCAI-test and non-MICCAI data. Results are presented as "averages ± standard deviations."

	Measure (Unit)	VOE (%)	RVD (%)	ASD (mm)	RMSD (mm)	MSD (mm)
MICCAI-test data	Healthy	4.2 ± 0.9	0.4 ± 0.9	0.6 ± 0.2	1.2 ± 0.4	14.2 ± 3.2
	Unhealthy	4.5 ± 0.6	0.2 ± 0.9	0.7 ± 0.1	1.2 ± 0.2	13.8 ± 2.9
Non-MICCAI data	Healthy	3.4 ± 0.9	0.4 ± 1.3	0.45 ± 0.2	0.9 ± 0.2	12.1 ± 3.3
	Unhealthy	2.9 ± 0.6	−0.1 ± 1.3	0.45 ± 0.2	1.02 ± 0.3	13.1 ± 4.3

TABLE IV. The p-value is obtained using a nonparametric test (Wilcoxon-Mann-Whitney rank sum test).

P-value	MICCAI and non-MICCAI	Healthy and unhealthy
VOE	0.0078[a]	0.2189
RVD	0.0614	0.2154
ASD	0.0206[a]	0.7039
RMSD	0.0688	0.3754
MSD	0.1973	0.8707

[a]Significant at $p < 0.05$.

TABLE V. Volumetry of segmented livers are measured for the MICCAI-training and non-MICCAI datasets. Results are compared with their references and shown as averages and standard deviations (SD) overall data.

	Region (unit)	Segmented liver (mm^3)	Reference (mm^3)	Overlapped (mm^3)
MICCAI-training data	Average	985 574	993 785	965 533
	SD	469 866	478 676	461 697
Non-MICCAI data	Average	1 403 595	1 396 071	1 369 084
	SD	685 589	671 926	670 059
Overall datasets	Average	1 284 160	1 281 132	1 253 784
	SD	656 325	645 925	641 291

However, the part of this muscle that is connected to the LIT and exists inside the boundary surface will be oversegmented (MICCAI-training 16).

In the portal phase, when the difference of intensity between most of the renal parenchyma and the liver is more than 20 HU. The kidney leakage to the liver was few enough not to affect the liver segmentation result. This is from our experience with the 80 datasets (MICCAI and non-MICCAI) used in this study. In late portal phase, the renal parenchyma may have almost same intensity as the liver. In this case, the region growing of kidneys is expected to leak into the liver parenchyma and the user has to separate them manually.

4.C. Segmenting LIT

Several approaches (Refs. 27, 38, and 40–42) for segmenting the liver from the portal phase result in undersegmentation of LITs. The proposed method is effective at segmenting LITs, as it classifies the histogram of the segmented core region of a LIT-liver into two components, one for the NLIT-part and the other for the LIT [Fig. 9(b)]. In a similar manner, the method classifies the core region of this LIT-liver into two partial core regions, one representing the core region of the NLIT-part and the other representing the core region of the LIT [Fig. 16(c)]. Each core region is extended based on its corresponding component [Sec. 2.C.3.b (Step 3.2)] [Fig. 16(d)]. Through reconfirmation of the boundary surface [Sec. 2.C.3.b (Step 3.2)], each contact region of NLIT- and LIT-results [Fig. 16(f)] is re-extended to complete segmentation of the liver [Fig. 16(g)]. In this step, muscles and LITs are mainly separated through stopping the contact region extension by the final boundary surface. During liver segmentation, the method separately identifies the NLIT- and the LIT-parts of LIT-livers in 3D [Fig. 16(h)].

When an LIT is small and is surrounded by BVs, it has two cases: (1) the LIT satisfies the intensity condition of Delaunay triangulation, this LIT is segmented with the core region and consequently with the liver [Figs. 16(a)–16(d) upper tumor]. (2) The LIT does not satisfy the intensity condition, this LIT will be a hole in the liver and will be segmented through filling holes at the refinement step and added to the liver. When a peripheral LIT is small and not surrounded by BVs at all, it will be undersegmented (MICCAI-test 1). Tumors that are small enough not to a distinguished as component in the mixture model will be segmented and classified in the NLIT-part of the liver.

4.D. Inter user variability

To avoid interuser variability, each interaction is followed by an automatic process that corrects this variability. For choosing the seed point of kidneys region growing [Sec. 2.B.1.a (Step 1)], an automatic correction is applied through replacing the chosen seed point by a 2D-region of

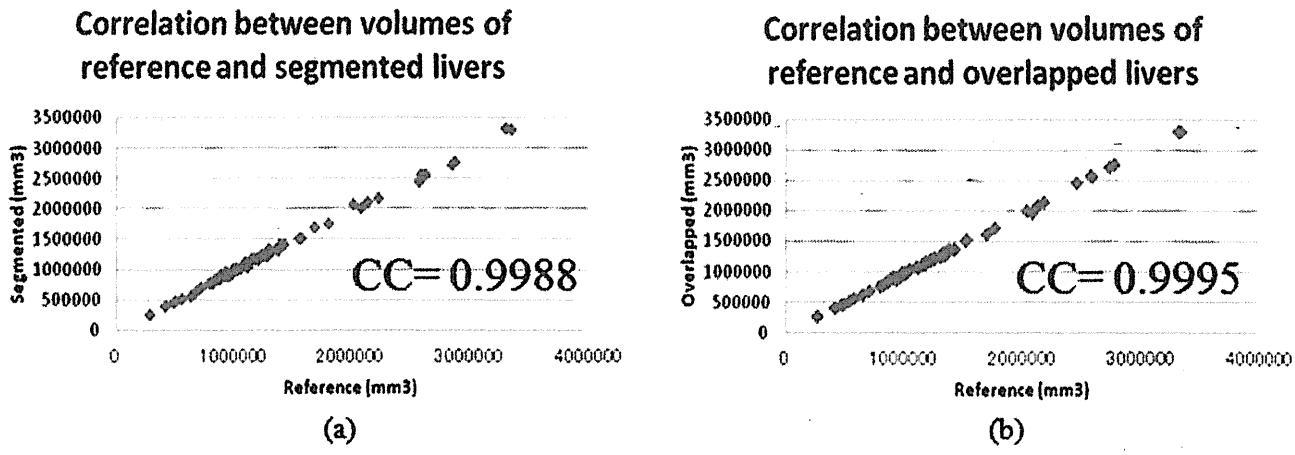

FIG. 14. Analysis of the relationship between segmented livers and their references using MICCAI-training and non-MICCAI data: (a) the correlation between volumes of segmented livers and their references and (b) the correlation between volumes of the overlapped liver regions and their corresponding references.

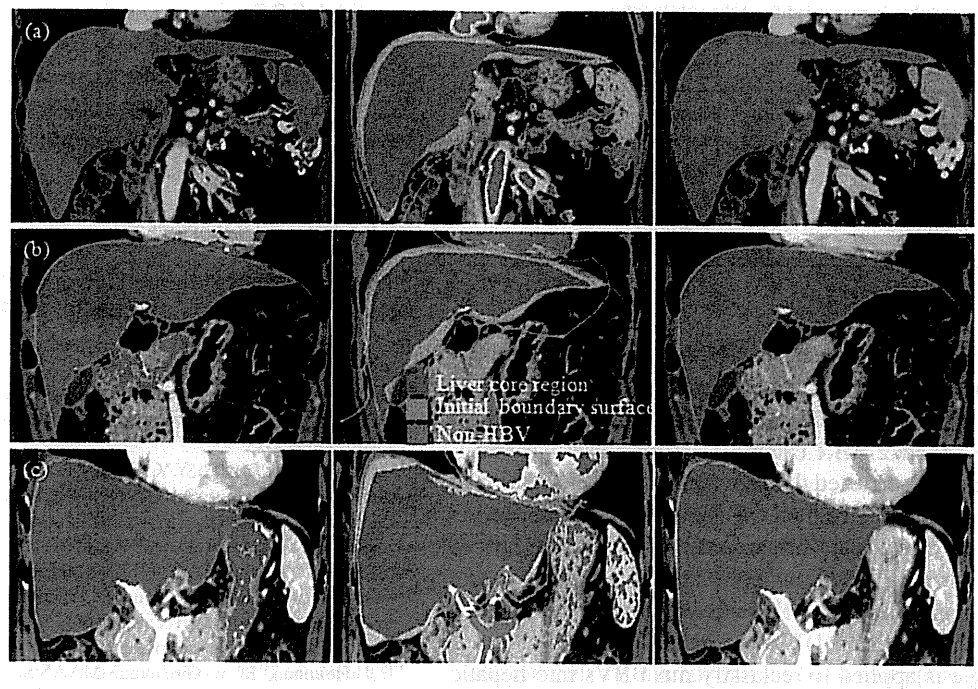

FIG. 15. Effectiveness of the constructed boundary surface at separating different organs neighboring the liver and having a similar intensity. (Left) Liver and other organs before constructing the boundary surfaces are illustrated (only the intensity variation condition is applied). (Middle) Core regions, non-HBVs cluster, and the constructed boundary surface are illustrated. (Right) Liver is separated from other organs in different cases by the boundary surface. (a) The spleen is separated. (b) The heart, pancreas, and intestines are separated in another case. (c) The stomach is separated in a third case (MICCAI - test 7).

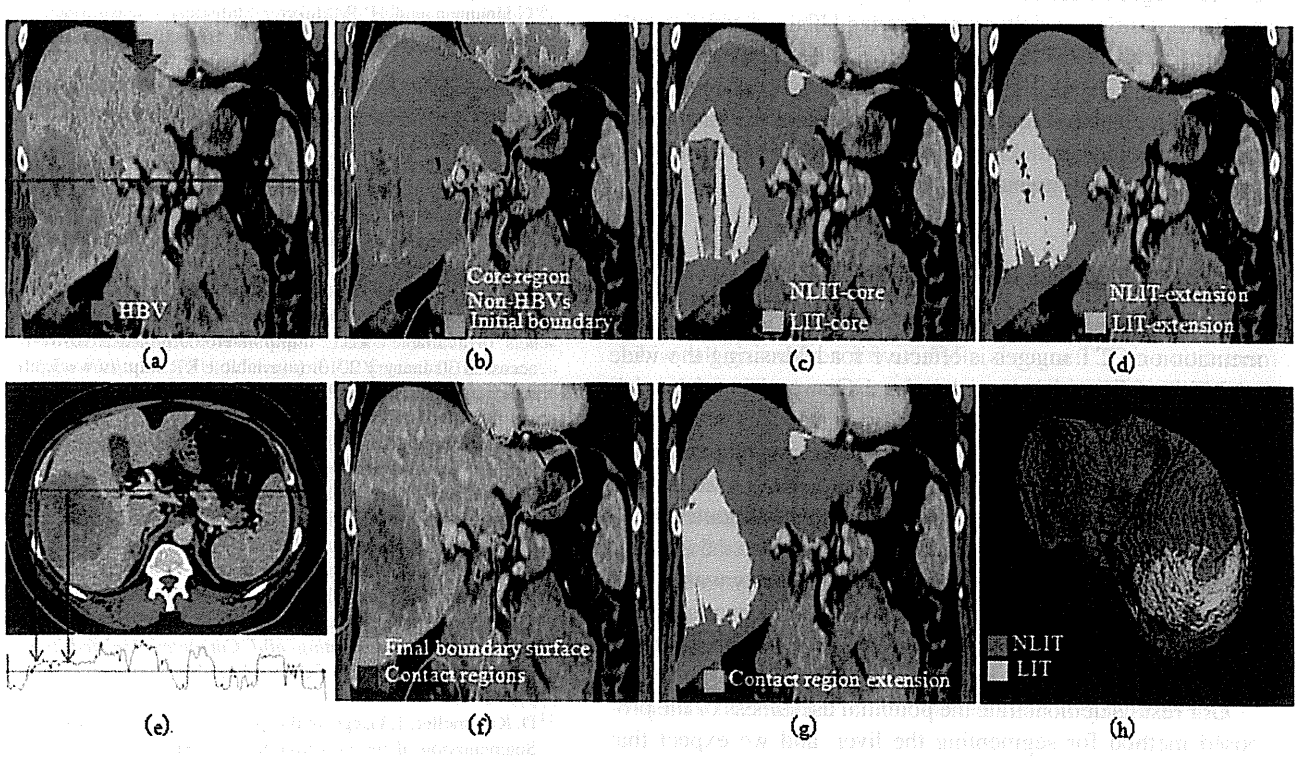

FIG. 16. Segmentation of a liver having a severe LIT: (a) HBVs surrounds the LIT [peripheral LITs are marked with arrows; (left) large LIT and (up) small LIT]. (b) Initial boundary surface is constructed between the core region and non-HBVs cluster. (c) Core region is classified into LIT- and NLIT-core regions. (d) Extensions of LITs and NLIT-cores are stopped by the initial boundary surface and intensity variation. (e) Muscles and LIT have nearly same intensity [position of this slice is marked with line in (a)]. (f) Contact regions of the first extension results and the initial boundary are illustrated with the final boundary surface. (g) The contact region in (f) is re-extended and stopped based on the final boundary and intensity variation. Holes are filled. (h) LIT and NLIT are illustrated in 3D.

TABLE VI. The p-value is measured from the results of two users.

P-value	Two users
VOE	0.1049
RVD	0.1949
ASD	0.1883
RMSD	0.8745
MSD	0.8785

radius 2 mm. Calculating the mean of intensities in this region, this mean is used as the actual threshold for the region growing. In choosing the seed point of blood vessel extraction region growing [Sec. 2.B.1.c (Step 3)], the interuser variability is automatically corrected through replacing the seed point with a 2D-region of radius 6 mm. The histogram of this region is calculated. The intensity corresponding to 75th percentile of these histograms is automatically chosen to be the actual threshold. In separating main blood vessels from abdominal BVs [Sec. 2.B.2.a (Step 1)], blood vessel refinement based on solid angle is applied to reclassify main BVs into hepatic and nonhepatic [Sec. 2.C.4 (Step 4)]. In order to verify the hypotheses that the method performance does not defer when applied by different users, p-value from a nonparametric test was measured for two users as in Table VI. This table demonstrates that the method is stable ($p > 0.05$) against interuser variability.

During reconfirmation of the initial boundary surface, the contact region between the boundary surface and the core region extension result was extended. This extension was stopped by the final boundary surface and intensity variation [Sec. 2.C.3.b (Step 3.2)]. It was noticed that: (1) where the first and the final boundary surfaces overlap, the contact region was not extended. (2) A very little region of the liver was under- or oversegmented.

5. CONCLUSIONS AND FUTURE WORK

This study demonstrates that the use of BVs in liver segmentation on CT images is effective for addressing the wide variability of liver shapes and sizes. Constructing a boundary surface using HBVs and non-HBVs is useful for separating the liver from its neighboring organs of similar intensity. By fitting the histogram of the core region using a variational Bayesian Gaussian mixture model, LIT can be segmented and quantitative measurement of NLIT- and LIT-parts of the liver becomes available. The proposed method's efficacy was evaluated using the standard MICCAI measures for liver segmentation and other standard measures of image segmentation for MICCAI and non-MICCAI data.

Our results demonstrate the potential usefulness of the proposed method for segmenting the liver, and we expect that this method may prove useful information to surgeons planning liver surgery and to other medical professionals working in clinical settings. Specifically, this method may provide important volumetric information about the liver and any associated hepatic tumors. The average processing time of the method is 9.7 min on a standard computer, which can be decreased by using multithreading processing. Based on deeper BV analysis, ABVs can be extracted and classified automatically. Thus, further developing the method so that it is fully automatic may be a worthwhile goal.

ACKNOWLEDGMENTS

This study was supported by a Grant-in-Aid for Scientific Research on Innovative Areas (21103005).

[a]Author to whom correspondence should be addressed. Electronic mail: niki@opt.tokushima-u.ac.jp; Telephone: +81886569430; Fax: +81886569433.

[1]F. Wang, K. T. Pan, S. Y. Chu, K. M. Chan, H. S. Chou, T. J. Wu, and W. C. Lee, "Preoperative estimation of the liver graft weight in adult right lobe living donor liver transplantation using maximal portal vein diameters," Liver Transplant. **17**, 373–380 (2011).

[2]S. Saito, J. Yamanaka, K. Miura, N. Nakao, T. Nagao, T. Sugimoto, T. Hirano, N. Kuroda, Y. Iimuro, and J. Fujimoto, "A novel 3D hepatectomy simulation based on liver circulation: Application to liver resection and transplantation," Hepatology **41**, 1297–1304 (2005).

[3]T. Heimann, B. v. Ginneken, M. A. Styner, Y. Arzhaeva, V. Aurich, C. Bauer, A. Beck, C. Becker, R. Beichel, G. Bekes, F. Bello, G. Binnig, H. Bischof, A. Bornik, P. M. Cashman, Y. Chi, A. Cordova, B. M. Dawant, M. Fidrich, J. D. Furst, D. Furukawa, L. Grenacher, J. Hornegger, D. Kainmüller, R. I. Kitney, H. Kobatake, H. Lamecker, T. Lange, J. Lee, B. Lennon, R. Li, S. Li, H. P. Meinzer, G. Nemeth, D. S. Raicu, A. M. Rau, E. M. V. Rikxoort, M. Rousson, L. Rusko, K. A. Saddi, G. Schmidt, D. Seghers, A. Shimizu, P. Slagmolen, E. Sorantin, G. Soza, R. Susomboon, J. M. Waite, A. Wimmer, and I. Wolf, "Comparison and evaluation of methods for liver segmentation from CT datasets," IEEE Trans. Med. Imaging **28**, 1251–1265 (2009).

[4]T. Heimann and H.-P. Meinzer, "Statistical shape models for 3D medical image segmentation: A review," Med. Image Anal. **13**(4), 543–563 (2009).

[5]P. Campadelli, E. Casiraghi, and A. Esposito, "Liver segmentation from computed tomography scans: A survey and a new algorithm," Artif. Intell. Med. **45**(2–3), 185–196 (2009).

[6]A. Schenk, G. Prause, and H. O. Peitgen, "Efficient semiautomatic segmentation of 3D objects in medical images," in *Proceedings of Medical Image Computing And Computer-Assisted Intervention (MICCAI) 2000*, Lecture Notes in Computer Science Vol. 1935 (Springer-Verlag, Berlin Heidelberg, 2000), pp. 71–131.

[7]A. Wimmar, G. Soza, and J. Hornegger, "Two-stage Semi-automatic Organ Segmentation Framework using Radial Bias Functions and Level sets" (available URL: http://sliver07.org/data/2010-01-14-1941.pdf), accessed 30 January 2013 or (available URL: http://www5.informatik.uni-erlangen.de/Forschung/Publikationen/2007/Wimmer07-TSO.pdf), accessed 30 January 2013.

[8]M. Kobashi and L. G. Shapiro, "Knowledge-based organ identification from CT images," Pattern Recognit. **28**(4), 475–491 (1995).

[9]D.-Y. Tsai and N. Tanahashi, "Neural-network-based boundary detection of liver structure in CT images for 3-D visualization," *Proceedings of IEEE International Conference on Neural Networks, IEEE Catalog No. 04CH37541* (Neural Networks, Orlando, FL, 1994), Vol. 6, pp. 3484–3489.

[10]T. Heimann, I. Wolf, and H. P. Meinzer, "Active shape models for a fully automated 3D segmentation of the liver—An evaluation on clinical data," *Medical Image Computing and Computer Assisted Intervention*, Lecture Notes in Computer Science Vol. 4191 (Springer, Heidelberg, 2006), pp. 41–48.

[11]D. Kainmuller, T. Lange, and H. Lamecker, "Shape Constrained Automatic Segmentation of the Liver based on a Heuristic Intensity Model" (available URL: http://www.sliver07.org/data/2007-10-22-1942.pdf), accessed 6 November 2012.

[12]A. Wimmer, G. Soza, and J. Hornegger, "A Generic Probabilistic Active Shape Model for Organ Segmentation" (available URL: http://www.sliver07.org/data/2009-03-11-0340.pdf), accessed 6 November 2012.

[13]L. Gao, D. G. Heath, and E. K. Fishman, "Abdominal image segmentation using three-dimensional deformable models," Invest. Radiol. **33**(6), 348–355 (1998).

[14]T. Okada, R. Shimada, Y. Sato, M. Hori, K. Yokota, M. Nakamoto, Y.-W. Chen, H. Nakamura, and S. Tamura, "Automated segmentation of the liver from 3D CT images using probabilistic Atlas and multi-level statistical shape model," *MICCAI 2007*, Lecture Notes in Computer Science Vol. 4791 (Springer-Verlag, Berlin Heidelberg, 2007), Part I, pp. 86–93.

[15]A. Wimmer, G. Soza, and J. Hornegger, "A generic probabilistic active shape model for organ segmentation," *MICCAI 2009*, Lecture Notes in Computer Science Vol. 5762 (Springer-Verlag Berlin, Heidelberg, 2009), Part II, pp. 26–33.

[16]J. Peng, "A new convex variational model for liver segmentation," *21st International Conference on Pattern Recognition (ICPR)*, (Pattern Recognition (ICPR), 2012 21st International Conference on, Tsukuba, 2012), pp. 3754–3757.

[17]M. Erdt, M. Kirschner, S. Steger, and S. Wesarg, "Fast automatic liver segmentation combining learned shape priors with observed shape Deviation," in *Proceedings of the IEEE International Symposium on Computer-Based Medical Systems (CBMS)* (Computer-Based Medical Systems (CBMS), 2010 IEEE 23rd International Symposium on, Perth, WA, 2010), pp. 249–254.

[18]K. Drechsler and C. O. Laura, "Simulation of portal vein clamping and the impact of safety margins for liver resection planning," *Abdominal Imaging. Computational and Clinical Applications Workshop Held on Conjunction with MICCAI 2011*, Lecture Notes in Computer Science Vol. 7029 (Springer-Verlag, Berlin Heidelberg, 2012), pp. 149–156.

[19]X. Zhou, T. Kitagawa, T. Hara, H. Fujita, X. Zhang, R. Yokoyama, H. Kondo, M. Kanematsu, and H. Hoshi, "Constructing a probabilistic model for automated liver region segmentation using non-contrast X-Ray TorsoCT images," *MICCAI 2006*, Lecture Notes in Computer Science Vol. 4191 (Springer-Verlag, Berlin Heidelberg, 2006), pp. 856–863.

[20]H. Park, P. H. Bland, and C. R. Meyer, "Construction of an abdominal probabilistic atlas and its application in segmentation," IEEE Trans. Med. Imaging **22**(4), 483–492 (2003).

[21]D. Furukawa, A. Shimizu, and H. Kobatake, "Automatic liver segmentation method based on maximum a posterior probability estimation and level set method," in *MICCAI 2007 Workshop Proceedings of the 3D Segmentation in the Clinic: A Grand Challenge* (2007), pp. 117–124.

[22]M. G. Linguraru, J. K. Sandberg, Z. Li, F. Shah, and R. M. Summers, "Automated segmentation and quantification of liver and spleen from CT images using normalized probabilistic atlases and enhancement estimation," Med. Phys. **37**(2), 771–783 (2010).

[23]L. Fernandez-de-Manuel, J. L. Rubio, M. J. Ledesma-Carbayo, J. Pascau, J. M. Tellado, E. Ramon, M. Desco, and A. Santos, "3D liver segmentation in preoperative CT images using a level-sets active surface method," Conf. Proc. IEEE Eng. Med. Biol. Soc. **2009**, 3625–3628 (2009).

[24]J. Lee, N. Kim, H. Lee, J. B. Seo, H. J. Won, Y. M. Shin, Y. G. Shin, and S. H. Kim, "Efficient liver segmentation using a level-set method with optimal detection of the initial liver boundary from level-set speed images," Comput. Methods Programs Biomed. **88**(1), 26–38 (2007).

[25]S. Pan and B. M. Dawant, "Automatic 3D segmentation of the liver from abdominal CT images: A level-set approach," Proc. SPIE **4322**, 128–138 (2001).

[26]R. Susomboon, D. S. Raicu, and J. Furst, "A hybrid approach for liver segmentation," in *Proceedings of MICCAI Workshop on 3D Segmentation in the Clinic: A Grand Challenge* (2007), pp. 151–160.

[27]L. Ruskó, G. Bekes, and M. Fidrich, "Automatic segmentation of the liver from multi- and single-phase," Med. Image Anal. **13**(6), 871–882 (2009).

[28]Y. Y. Boykov and M.-P. Jolly, "Interactive graph cuts for optimal boundary & region segmentation of objects in N-D images," Proc. Int. Conf. Comput. Vis. **I**, 105–112 (2001).

[29]Y. Boykov and G. Funka-Lea, "Graph cuts and efficient N-D image segmentation," Int. J. Comput. Vis. **70**(2), 109–131 (2006).

[30]R. Beichel, C. Bauer, A. Bornik, E. Sorantin, and H. Bischof, "Liver segmentation in CT data: A segmentation refinement approach," *3D Segmentation in the Clinic: A Grand Challenge* (2007), pp. 235–245.

[31]A. Afifi and T. Nakaguchi, "Liver segmentation approach using graph cuts and iteratively estimated shape and intensity constrains," *Proceedings of the 15th Conference on Medical Image Computing and Computer-Assisted Intervention (MICCAI)* (Springer-Verlag, Berlin Heidelberg, 2012), Pt. 2, pp. 395–403.

[32]L. Massoptier and S. Casciaro, "Fully automatic liver segmentation through graph-cut technique," *Proceedings of the 29th Annual International Conference of the IEEE -EMBS* (Engineering in Medicine and Biology Society, 2007, EMBS 2007, 29th Annual International Conference of the IEEE, Lyon, 2007), pp. 5243–5246.

[33]S. Esneault, N. Hraiech, E. Delabrousse, and J.-L. Dillenseger, "Graph cut liver segmentation for interstitial ultrasound therapy," *Conference Proceedings of the International Conference of IEEE Engineering in Medicine and Biology Society* (Engineering in Medicine and Biology Society, 2007, EMBS 2007, 29th Annual International Conference of the IEEE, Lyon, 2007), pp 5247–5250.

[34]Y. Chen, W. Zhao, Q. Wu, Z. Wang, and J. Hu, "Liver segmentation in CT images for intervention using a graph-cut based model," *Abdominal Imaging. Computational and Clinical Applications Workshop Held on Conjunction with MICCAI 2011*, Lecture Notes in Computer Science Vol. 7029 (Springer-Verlag, Berlin Heidelberg, 2012), pp. 157–164.

[35]M. G. Linguraru, W. J. Richbourg, J. M. Watt, V. Pamulapati, and R. M. Summers, "Liver and tumor segmentation and analysis from CT of diseased patients via a generic affine invariant shape parameterization and graph cuts," *Abdominal Imaging 2011*, Lecture Notes in Computer Science Vol. 7029 (Springer-Verlag, Berlin Heidelberg, 2012), pp. 198–206.

[36]V. Pamulapati, A. Venkatesan, B. J. Wood, and M. G. Linguraru, "Liver segmental anatomy and analysis from vessel and tumor segmentation via optimized graph cuts," *Abdominal Imaging 2011*, Lecture Notes in Computer Science Vol. 7029 (Springer-Verlag, Berlin Heidelberg, 2012), pp 198–206.

[37]M. G. Linguraru, W. J. Richbourg, J. Liu, J. M. Watt, V. Pamulapati, S. Wang, and R. M. Summers, "Tumor burden analysis on computed tomography by automated liver and tumor segmentation," IEEE Trans. Med. Imaging **31**(10), 1965–1976 (2012).

[38]D. A. Oliveira, R. Q. Feitosa, and M. M. Correia, "Segmentation of liver, its vessels and lesions from CT images for surgical planning," Biomed. Eng. Online (available URL: http://www.biomedical-engineering-online.com/content/10/1/30), accessed 30 September 2013.

[39]S.-J. Lim, Y.-Y. Jeong, and Y.-S. Ho, "Automatic liver segmentation for volume measurement in CT Images," Vis. Commun. Image Represent. **17**(4), 860–875 (2006).

[40]G. Schmidt, M. Athelogou, R. Schönmeyer, R. Korn, and G. Binnig, "Cognition network technology for a fully automated 3D segmentation of liver," in *MICCAI 2007 Workshop Proceedings of the 3D Segmentation in the Clinic: A Grand Challenge* (2007), pp. 125–134.

[41]K. A. Saddi, M. Rousson, C. C. hotel, and F. Cheriet, Global-to-local shape matching for liver segmentation in CT imaging. in *MICCAI 2007 Workshop Proceedings of the 3D Segmentation in the Clinic: A Grand Challenge* (2007), pp. 207–214.

[42]W. N. J. W. Yussof and H. Burkhardt, "Automatic 3D liver segmentation using morphological operations and graph-cut techniques," Journal of Next Generation Information Technology **2**(3), 23–34 (2011).

[43]A. S. Maklad, M. Matsuhiro, H. Suzuki, Y. Kawata, N. Niki, T. Utsunomiya, and M. Shimada, "Blood vessel-based liver segmentation through the portal phase of a CT dataset," Proc. SPIE **8670**, 86700X-1–86700X-7 (2013).

[44]A. S. Maklad, M. Matsuhiro, H. Suzuki, Y. Kawata, N. Niki, T. Utsunomiya, and M. Shimada, "Extraction of liver volumetry based on blood vessel from the portal phase CT dataset," Proc. SPIE **8314**, 83142O-1–83142O-7 (2012).

[45]T. Saitoh, Y. Tamura, and T. Kaneko, "Automatic segmentation of liver region based on extracted blood vessels," Syst. Comput. Jpn. **35**(5), 1–10 (2004) [Denshi Joho Tsushin Gakkai Ronbunshi **J86-D-II**(5), 633–641 (2003)].

[46]I. R. Francis, R. H. Cohan, N. J. McNulty, J. F. Platt, M. Korobkin, A. Gebremariam, and K. I. Ragupathi, "Multidetector CT of the liver and hepatic neoplasms: Effect of multiphasic imaging on tumor conspicuity and vascular enhancement," AJR, Am. J. Roentgenol. **180**(5), 1217–1224 (2003).

[47]A. Oto, K. Kulkarni, R. Nishikawa, and R. L. Baron, "Contrast enhancement of hepatic heangiomas on multiphase MDCT: Can we daiagnose hepatic hemangiomas by comparing enhancement with blood pool?," AJR, Am. J. Roentgenol. **195**(2), 381–386 (2010).

[48]B. V. Ginnekan, T. Heimann, and M. Styner, "3D Segmentation in the clinic: A grand challenge," in *MICCAI 2007 Workshop Proceedings of the 3D Segmentation in the Clinic:A Grand Challenge* (American Roentgen Ray Society, 2007), pp 7–15.

[49]I. Pitas, *Digital Image Processing Algorithms and Applications* (Wily Inter Science, U.S.A., 2000).

[50]A. Fabijanska "Results of applying a two-path region growing algorithm for airway tree segmentation to MDCT chest scans from EXACT database," *EXACT09* (2009), pp. 251–260 (available URL: http://image.diku.dk/exact/result/VOLCED_description.pdf), accessed 2 July 2013.

[51]S. W. Smith, *The Scientist and Engineer's Guide to Digital Signal Processing*, 2nd ed., (California Technical Publishing, San Diego, 1997–2011), Chap. 25, pp 436–442 (available URL: http://www.dspguide.com/CH25.PDF), accessed 9 October 2012.

[52]J. Toriwaki and H. Yoshida, *Fundamentals of Three-Dimensional Digital Image Processing* (Springer-Verlag London Limited, 2009), Sec. 5.

[53]E. Takahashi, Y. Kawata, N. Niki, Y. Nakano, M. Harada, and N. Moriyama, "Computer aided diagnosis for osteoporosis based on vertebral column structure analysis," Proc. SPIE **8315**, 831533 (2012).

[54]D. F. Watson, "Computing the n-dimensional Delaunay tessellation with application to Voronoi polytopes," Comput. J. **24**(2), 167–172 (1981).

[55]K. Palágyi, J. Tschirren, E. A. Hoffman, and M. Sonka, "Quantitative analysis of pulmonary airway tree structures," Comput. Biol. Med. **36**(9), 974–996 (2006).

[56]C. M. Bishop, *Pattern Recognition and Machine Learning* (Springer Science+Business Media, LLC, Singapore), Sec. 10.

[57]S. O'Brien, "Computing the Solid Angle of Two Detectors Using Monte Carlo Methods" (available URL: http://acadine.physics.jmu.edu/group/technical_notes/Solid_angle_latex/solid_angle.pdf), accessed 18 December 2012.

[58]P. Dalgaard, *Statistics and Computing: Introductory Statistics with R* (Springer-Verlag, New York, 2002).

Cancer Chemother Pharmacol (2013) 72:463–470
DOI 10.1007/s00280-013-2222-x

ORIGINAL ARTICLE

A multi-institutional phase II trial of hepatic arterial infusion chemotherapy with cisplatin for advanced hepatocellular carcinoma with portal vein tumor thrombosis

Masafumi Ikeda · Takuji Okusaka · Junji Furuse · Shuichi Mitsunaga · Hideki Ueno · Hidekazu Yamaura · Yoshitaka Inaba · Yoshito Takeuchi · Mitsuo Satake · Yasuaki Arai

Received: 11 February 2013 / Accepted: 16 June 2013 / Published online: 29 June 2013

Abstract
Purpose The objective of this study was to evaluate the response rate, survival, and adverse effects of hepatic arterial infusion chemotherapy (HAIC) using cisplatin in patients with advanced hepatocellular carcinoma (HCC) and portal vein tumor thrombosis (PVTT).
Methods Twenty-five patients of advanced HCC with PVTT in the main or first branch, having no prior history of chemotherapy, measurable lesions, adequate liver and renal function, and adequate bone marrow reserve, were enrolled. Cisplatin was administered at the dose of 65 mg/m^2 via the proper hepatic artery. Treatment was repeated every 4–6 weeks for a maximum of six courses until the appearance of evidence of tumor progression or unacceptable toxicity.
Results The median number of treatments was 3 (range 1–6). Among the 25 enrolled patients, complete response was achieved in 1 (4 %) patient and partial response in 6 (24 %), corresponding to a response rate of 28 % (95 % CI 12–49 %). The median progression-free and overall survival times and the 1-, 2-, and 3-year survival rates in the enrolled patients were 3.6 and 7.6 months and 40.3, 36.0, 20 %, respectively. Four of the seven patients who showed complete or partial response survived for more than 3 years. The main grade 3/4 non-hematological adverse events of this treatment were elevation of the serum aspartate aminotransferase (44 %) and alanine aminotransferase (24 %).
Conclusion HAIC with cisplatin exerts moderate activity with mild toxicity in advanced HCC patients with PVTT. Especially, markedly prolonged survival can be expected in patients who respond to this treatment.

Keywords Hepatocellular carcinoma · Hepatic arterial infusion chemotherapy · Tumor thrombosis · Cisplatin · Clinical trial

Abbreviations

HCC	Hepatocellular carcinoma
PVTT	Portal vein tumor thrombosis
HAIC	Hepatic arterial infusion chemotherapy
AFP	Alpha-fetoprotein
PIVKA II	Protein induced by vitamin K absence or antagonist-II
AST	Aspartate aminotransferase
ALT	Alanine aminotransferase

M. Ikeda · T. Okusaka · H. Ueno
Hepatobiliary and Pancreatic Oncology Division, National Cancer Center Hospital, Tokyo, Japan

M. Ikeda (✉) · J. Furuse · S. Mitsunaga
Division of Hepatobiliary and Pancreatic Oncology, National Cancer Center Hospital East, Kashiwa, Japan
e-mail: masikeda@east.ncc.go.jp

J. Furuse
Department of Internal Medicine, Medical Oncology, Kyorin University School of Medicine, Tokyo, Japan

H. Yamaura · Y. Inaba
Department of Interventional and Diagnostic Radiology, Aichi Cancer Center, Nagoya, Japan

Y. Takeuchi · Y. Arai
Division of Diagnostic Radiology, National Cancer Center Hospital, Tokyo, Japan

M. Satake
Division of Diagnostic Radiology, National Cancer Center Hospital East, Kashiwa, Japan

Introduction

For advanced hepatocellular carcinoma (HCC) patients with portal vein tumor thrombosis (PVTT), chemotherapy remains one of the most important treatment modalities [1–4]. Sorafenib, an oral multikinase inhibitor targeting Raf kinase and receptor tyrosine kinases, has been acknowledged as the standard agent for advanced HCC [5, 6]. However, it has yielded rather unsatisfactory results in terms of the response and survival in patients with advanced HCC [7, 8]. Hepatic arterial infusion chemotherapy (HAIC), which can increase the local concentration of anticancer drugs with reduced systemic distribution, may be expected to exert better antitumor efficacy and lesser toxicity [9, 10]. Although promising results of HAIC have been reported for advanced HCC with PVTT [11–20], no chemotherapeutic agent or regimen has yet been shown to confer a survival benefit sufficient for adoption as standard therapy.

Cisplatin, which is a heavy metal (platinum) ion complex compound that exerts cytotoxicity by binding to double-stranded DNA, is widely used as one of the chemotherapeutic agents in transcatheter arterial embolization [21–23]. Cisplatin in the form of a fine powder suitable for hepatic artery infusion (IA-call®, Nippon Kayaku Co., Ltd.) has been developed in Japan. Since the solubility of this agent is 2.86 times higher than that of standard cisplatin, the injection time can be shortened. In a phase II trial, administration of this agent by intra-arterial injection over 20–40 min at the dose of 65 mg/m^2 in repeated doses at 4- to 6-week intervals was shown to yield favorable results (response rate 33.8 %) [24]. However, the efficacy of this regimen for advanced HCC with PVTT has not yet been fully evaluated. Therefore, we conducted a multicenter phase II trial to evaluate the efficacy and safety of HAIC with cisplatin in HCC patients with PVTT in the main and/or first branch.

Patients and methods

Eligibility

Patients eligible for study entry had advanced HCC with PVTT. The eligibility criteria were as follows: HCC confirmed by histological examination or liver tumor with a radiological hallmark of HCC and elevation of the serum α-fetoprotein (AFP) levels to ≥400 ng/mL; tumor thrombosis in the main and/or first portal vein; unsuitable candidate for surgical resection; age 20 years or over; Eastern Cooperative Oncology Group performance status of 0–2; measurable disease; interval of 4 weeks or over between the last treatment and the present therapy, and no influence of previous treatments; adequate hematological function (hemoglobin ≥9.0 g/dL, leukocytes ≥3,000/mm^3, and platelets ≥50,000/mm^3), adequate hepatic function [Child-Pugh classification of A or B, serum total bilirubin ≤2.0 mg/dL, and serum aspartate aminotransferase (AST)/alanine aminotransferase (ALT) ≤150 U/L], adequate renal function (serum creatinine ≤1.1 mg/dL); availability of written informed consent.

The exclusion criteria were as follows: prior chemotherapy with cisplatin for HCC, prior radiotherapy, transcatheter arterial chemoembolization or intra-arterial chemotherapy for PVTT, refractory pleural effusion or ascites, no distant metastases, allergic reaction to iodine contrast medium, severe renal, heart or mental disease, active infection, excluding hepatitis B or C viral infection, active concomitant malignancy, pregnant and lactating females; females of childbearing age unless using effective contraception.

The pretreatment evaluation consisted of a complete history and physical examination and baseline assessments of organ function. In addition, dynamic computed tomography of the abdomen and chest radiography were performed for pretreatment staging to assess the local extent of the tumor and exclude the presence of distant metastasis. The number of tumors and tumor distribution were examined by computed tomography and/or angiography. This phase II study was conducted with the approval of each institutional review board and conducted in accordance with the Declaration of Helsinki.

Treatment procedure

Following conventional visceral angiography, HAIC was performed by introducing a angiographic catheter into the proper, right or left hepatic artery, or another feeding artery, and injection of cisplatin at the dose of 65 mg/m^2 over 20–40 min by Seldinger's technique, not using implanted port system for hepatic arterial infusion chemotherapy. Until the appearance of evidence of tumor progression and/or unacceptable toxicity, the treatment was repeated every 4–6 weeks for a maximum of six cycles. Neither lipiodol nor gelatin sponge was allowed in the protocol treatments. Antiemetic prophylaxis with a 5-HT3 antagonist (granisetron 1 mg) plus dexamethasone 8 mg was used at the attending physician's discretion. Patients received adequate hydration and/or diuretics for protection against cisplatin-induced renal dysfunction, and the urine output was carefully monitored, especially during the first 3 days after intra-arterial administration of cisplatin. The cisplatin dose was reduced in case of grade 4 hematological adverse events or serious events had developed during the previous cycle. Patients who were refractory to this treatment regimen were allowed to

receive other anticancer treatments at the attending physician's discretion.

Response and toxicity assessment

The antitumor effect was assessed by intravenous contrast enhanced computed tomography or magnetic resonance imaging every 4–6 weeks. Responses were evaluated according to the WHO criteria [25]. The best overall response was recorded for each patient. The duration of response was defined as the interval from the onset of partial response until the first evidence of disease progression or death. Basic laboratory tests, including a complete blood count with differential leukocyte count, and serum chemistry were performed at least once every 2 weeks during this treatment. The treatment-related adverse events were assessed using the Common Terminology Criteria for Adverse Events, v2.0. Serum levels of AFP and protein induced by vitamin K absence or antagonist-II (PIVKA II) were measured every 4–6 weeks. In patients with a pretreatment AFP level of $\geq$100 ng/mL and of PIVKAII of $\geq$100 mAU/mL, the AFP and PIVKAII responses were assessed; a positive response was defined as a >50 % reduction from the pretreatment level. Progression-free survival was defined as the time from the date of initial treatment to the first documentation of progression or death. Overall survival was measured from the date of initial treatment to the date of death or the date of the last follow-up. The progression-free survival and overall survival curves were calculated by the Kaplan–Meier method.

Statistical considerations

The primary endpoint of this trial was the response rate, and the secondary endpoints were adverse events, progression-free survival, and overall survival. The number of patients enrolled was planned using a two-step design [26] based on an expected response rate of 30 %, a response rate corresponding to no activity of 10 %, α error of 10 %, and β error of 10 %. An interim analysis was planned after 15 patients had been enrolled. If zero or one of the first 15 patients showed a partial response or complete response, the study was to be ended. If a response was detected in more than one of the first 15 patients studied, an additional 10 patients were to be enrolled in a second stage of accrual for more precise estimation of the actual response rate. If a response was detected in more than five of the 25 patients studied, this treatment was considered to be effective. This population was defined as including any patients who received at least one course of study medication. The trial was registered at UMIN-CTR (http://www.umin.ac.jp/ctr/index-j.htm), identification number (UMIN000000488).

Results

Patient characteristics

Twenty-five patients were enrolled in this trial between January 2005 and April 2007 at 3 institutions in Japan, because four patients showed partial response among the first 15 patients in the interim analysis. The characteristics of all the 25 patients are shown in Table 1. There were 20 males and five females, with a median age of 67 (range 47–79) years. Hepatitis B surface antigen and hepatitis C virus antibody were positive in 4 patients (16 %) and 15 patients (60 %), respectively. There were 17 (68 %) patients and 8 (32 %) patients with Child-Pugh class A and B, respectively. Portal vein invasion was noted in the main vein and the first branch in 19 patients (76 %) and 6 (24 %) patients, respectively.

A total of 83 courses were given, with a median of three courses (range 1–6) per patient. The median dose of cisplatin per treatment was 100 mg (range 85–130 mg). The reasons for treatment discontinuation were completion of treatment (6 courses) in 5 patients (20 %), disease progression in 16 patients (64 %), rupture of esophageal varices in 1 patient (4 %), hepatic failure in 1 patient (4 %), and accidental perforation of the colon in 1 patient (4 %). As subsequent treatments, 15 patients did not receive any treatments and the remaining 10 patients received further treatment: HAIC with epirubicin (4 patients), HAIC with interferon plus 5-fluorouracil (5-FU) (1 patient), HAIC with cisplatin (2 patients who had shown disease progression after the termination of 6 cycles of HAIC with cisplatin), and transcatheter arterial chemoembolization with epirubicin (2 patients).

Treatment efficacy

Of the 25 patients, 24 were evaluable for response; the remaining one patient (4 %) could not be evaluated because of early discontinuation of this protocol treatment. One patient (4 %) showed complete response, and 6 (24 %) showed partial response, corresponding to an overall response rate of 28 % (95 % CI 12–49 %); the mean duration of the response was 7.9 months (range 1.4–19.5 months). Eleven patients (44 %) showed stable disease and 5 patients (20 %) showed progressive disease. During the treatment, the serum AFP level decreased by more than 50 % in 7 (44 %) of the 16 patients with a pretreatment level of $\geq$100 U/mL, and the serum PIVKA II level decreased by more than 50 % in 15 (68 %) of the 22 patients with a pretreatment level of $\geq$100 mAU/mL.

At the time of the analysis, 21 patients developed tumor progression; among the remaining 4 patients, the tumor progression status could not be confirmed in 3 patients (on